文章编号：0258-7025(2009)12-3093-23

Diffractive Multi-beam Ultra-fast Laser Micro-processing Using a Spatial Light Modulator

(Invited Paper)

Zheng Kuang Dun Liu* Walter Perrie Jian Cheng Shuo Shang S. P. Edwardson E. Fearon G. Dearden K. G. Watkins

(*Laser Group*, *Department of Engineering*, *University of Liverpool*, *Brownlow Street*, *Liverpool*, *L*69 3*GQ*, *UK*)

Corresponding author: *dun.liu@liv.ac.uk*

Received October 28, 2009

Abstract Multi-beam ultra-fast laser parallel microprocessing using spatial light modulation is demonstrated in this paper. Diffractive multi-beam patterns are generated with a spatial light modulator (SLM), which is driven by computer generated holograms (CGHs). The CGHs calculated by appropriate algorithms are displayed on the SLM to split an input laser beam to a number of beamlets and digitally manipulate their positions and intensity. The undesired damage by the energetic zero order beam can be avoided by either installing a 4*f* optical system to block the zero order at the Fourier plane or adding a Fresnel zone lens on the CGH to defocus the zero order at the processing plane. The surface ablation of materials using multi-beam patterns synchronised with a scanning galvanometer system shows flexible and high throughput parallel processing. By tightly focusing the diffractive beams with an objective into transparent materials, high speed dynamic femto-second laser two-dimensional (2D) and three-dimensional (3D) internal structuring is also presented. The results demonstrate the high precision micro-processing with higher efficiency, showing the potential for ultra-fast laser parallel processing in real industrial applications.

Key words femto-second laser; spatial light modulator (SLM); computer generated holograms (CGH).

CLCN: O484 **Document Code**: A **doi**: 10.3788/CJL20093612.3093

1 Introduction

During the last decade, ultra-fast lasers have been employed to obtain micro-processing of materials including both high precision surface micro-machining and three-dimensional (3D) internal structuring. Due to the ultra-high intensity of focussed femto-second pulses ($I>10^{12}$ W/cm^2) non-linear absorption can be induced at the focus, leading to highly localized material ablation or modification[1~7]. In metals, when the input fluence, F, is kept in the low regime, a few times above the ablation threshold ($F\sim1$ J/cm^2), heat diffusion during the temporal ultra-short pulse width can be reduced to the nano-meter scale, comparable to the optical skin depth[8~10]. Accordingly, the pulse energy used in ultra-fast laser processing is often kept to the micro-joule (μJ) level for fine micro/nano-surface structuring due to the low and well-defined ablation thresholds. Consequently, high gain regenerative amplifier systems running at repetition rate of about 1 kHz, providing milli-joule (mJ) level output pulse energy have to be attenuated severely, thus limiting the useful throughput.

Generating parallel multi-beam, by spatially splitting a mJ level energy laser pulse into many lower energy μJ laser pulses, is a novel and straightforward method to increase the efficiency and throughput of precision ultra-fast laser processing. From multi-beam interference[11~25] to micro-lens arrays[26~31], previous studies have demonstrated a number of approaches to create multi-beam to improve ultra-fast laser micro-fabrication. Parallel processing with arbitrary multi-beam patterns using a spatial light modulator (SLM) as a dynamic device of diffractive optical elements was first employed by Hayasaki *et al*.[32~39]. In this paper, dynamic femto-second and pico-second laser highly parallel processing using SLMs with scanning galvanometers is demonstrated, clarifying the importance of laser bandwidth[40~43]. High average power pico-second processing up to 1.2 W into diffractive beams is also reported, signifying the potential of this technique in industrial applications. In addition, dynamic femto-second laser parallel refractive index two-dimensional (2D) and 3D structuring inside transparent materials is carried out. As a result, high quality volume gratings are produced with a gain factor G over 20. Finally, a series of applications are demonstrated, showing great potential for applying this technique in industry.

2 Generation of Multiple Beams Using a SLM

2.1 Introduction to SLM

Figure 1 is a sketch showing how a SLM works, in which the input light is modulated by the hologram displayed on the SLM after (a) reflection or (b) transmission. The signal transmitting the holograms can be either optical or electrical, depending on the type of SLM. Electrical addressed reflective SLMs (ER-SLMs), Holoeye[44] LC-R 2500 and Hamamatsu[45] X10468 series, are employed in our research.

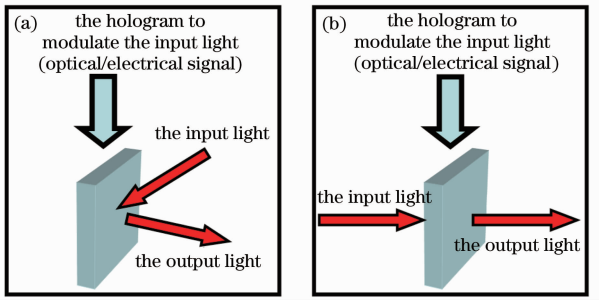

Fig. 1 Sketches demonstrating different types of SLMs. (a) reflective; (b) transmissive, and how they work

Most of ER-SLMs have a nematic liquid crystal display (LCD) where holograms can be presented. Figure 2 schematically shows the basic structure of LCD. The charge-coupled device (CCD) chip on the left of the figure, having a pixelated 2D array structure with a given resolution (1024 × 768 for Holoeye LC-R 2500 SLM[44]), is a device to electrically load the data from the computer generated holograms (CGHs) which has the same resolution. After the data is transmitted, the required voltage is addressed onto each of the pixels to build up an electric field, E, leading to a series of changes on the corresponding liquid crystal (LC), e. g., refractive index change, Δn[46, 47]. As shown on the right of the figure, the input light firstly reaches a transparent protective glass layer and then a transparent electrode, normally made of indium tin oxide (ITO). Then with reflection at the mirror, the light goes through the LC layer for a second time. The phase of the output light is modulated mainly due to Δn, driven by the electric field, E.

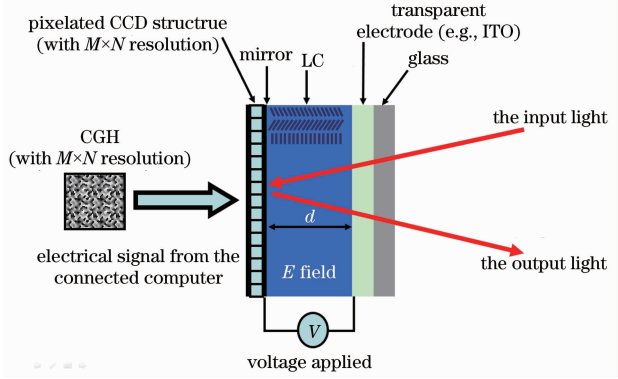

Fig. 2 Basic structure of a LCD

2.1.1 Phase Modulation

The optical path difference (δ) and the phase change ($\Delta\varphi$) of the output light can be evaluated by the following equations:

$$\delta \approx 2\Delta nd, \tag{1}$$

$$\Delta\varphi = k \cdot \delta \approx \frac{2\pi}{\lambda} 2\Delta nd = \frac{4\pi}{\lambda}\Delta nd, \tag{2}$$

where k and λ are the wave number and wavelength of the input light respectively, and d is the thickness of the LC. Since Δn is a function of the voltage (v), i.e., $\Delta n = f(v)$. Thus

$$\Delta\varphi \approx \frac{4\pi}{\lambda} d \cdot f(v). \tag{3}$$

Since the commercial SLM displays a 8-bit CGH, where the change of voltage driven by the CCD pixels has $2^8 = 256$ levels, normally symbolized by the 0～255 grey levels, the phase change ($\Delta\varphi$) is a function of the grey level. The graph of $\Delta\varphi$ versus grey level as shown in Fig. 3, which is from the measured results of the Holoeye LC-R 2500 SLM with $\lambda = 632.8$ nm linearly polarized laser input[48], demonstrates near linear increase of the phase modulation by changing the grey levels from 0 to 255.

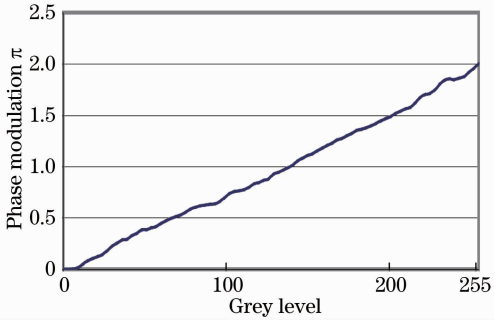

Fig. 3 Measured results of Holoeye LC-R 2500 SLM with $\lambda = 632.8$ nm linearly polarized laser input, showing near linear increase of the phase modulation by changing the grey levels from 0 to 255[48]

2.1.2 Intensity Modulation

The polarization of the output light can also changed by the voltage, i.e., the grey level. So, with the setup shown in Fig. 4, (where two polarizers, P and A, with perpendicular polarisation direction, are installed before the light illuminating and after reflecting on the SLM, respectively), intensi-

ty modulation can be obtained. The intensity measured after the analyzer (A) depend on the grey level driving the voltage through the pixels to twist the LC cells.

Overall, as shown in Fig. 5, an SLM is able to modulate both phase (φ_0) and amplitude (A_0) of the input light by using the appropriate setup and CGH.

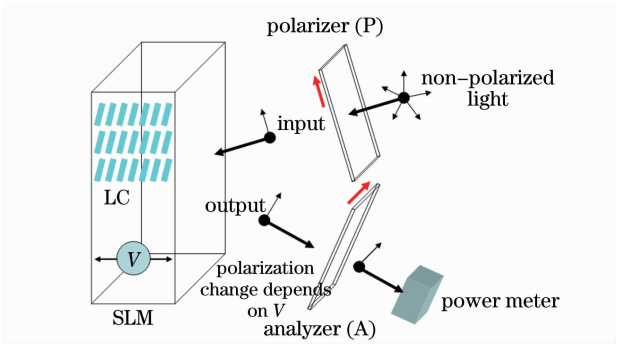

Fig. 4 Setup for intensity modulation

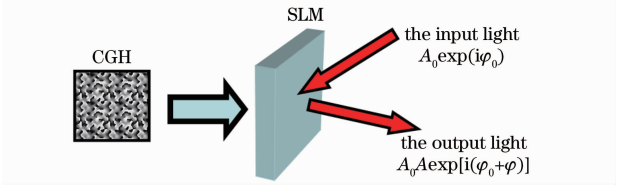

Fig. 5 Schematic illustration of how a SLM works-modulating the phase/intensity of the light

2.2 Generation of Multiple Beams with an SLM

With an SLM, phase holograms are widely used to generate multiple beams for different applications from multi-trapping of micro-particles in optical tweezers[49~64] to ultra-fast laser material micro-processing[32~43], while intensity holograms have other applications, e.g., laser beam shaping, where the hologram works as an intensity mask to modulate the intensity distribution of the input laser beam[65, 66]. Generally speaking, according to a positional relationship between the hologram and the target, the phase holograms used to generate multiple beams can be classified into three different types.

The first type is the Fourier plane hologram, because the target is put on the Fourier plane of the hologram, as shown in Fig. 6, where lenses 1 and 2 forms a 4*f*-imaging optical system, and the un-diffracted zero beam is simply blocked with a spatial filter and lens 3 is actually used to focus the diffracted multiple beams at the Fourier plane for the application. Based on a Fourier transform, the iterative Gerchberg-Saxton (GS) algorithm[67], widely used in various applications from holographic optical

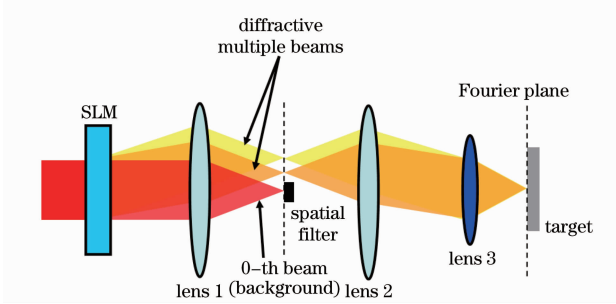

Fig. 6 Creation of multiple beams with Fourier plane hologram

tweezers to ultra-fast laser parallel micro-processing[32,50], is probably the most popular method to calculate this type of CGH. An algorithm with a non-iterative approach, the superposition of prisms, first published by Liesener *et al*.[54] is another method to generate Fourier plane hologram, and this has demonstrated some improvement over the GS algorithm, e.g., the calculation speed[68]. Both of the algorithms have been employed in the current study.

The Fresnel plane hologram is the second type, where the target is put on the Fresnel plane of the hologram. Figure 7 demonstrates the positional relationship between this hologram and the target, where the diffracted beams are focused on the Fresnel plane by the hologram, with lenses 1 and 2 employed as a telescope system. The un-modulated zero order beam is in the background of the diffracted peaks, with no influence on the target. Multi-plexed phase Fresnel lenses hologram, first attempted by Satoshi Hasegawa *et al*. to generate multiple focused peaks for holographic femto-second laser processing[33,38], is a typical Fresnel plane hologram.

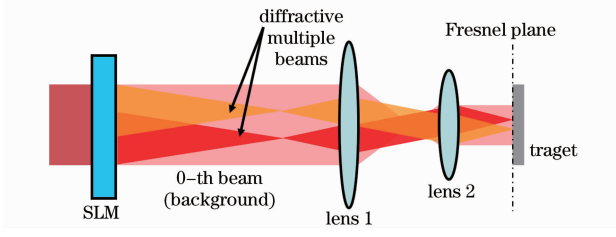

Fig. 7 Create multiple beams with Fresnel plane hologram

The third type is a combination of the Fourier and Fresnel plane holograms. As illustrated in Fig. 8, with this type of hologram, the target is put on a plane, which is neither the Fourier nor the Fresnel plane, but is placed where the multiple diffractive beams focus. Since the zero order beam is defocused on the target plane, this type of hologram can

be used to avoid the un-wanted effects caused by the zero order beam[42].

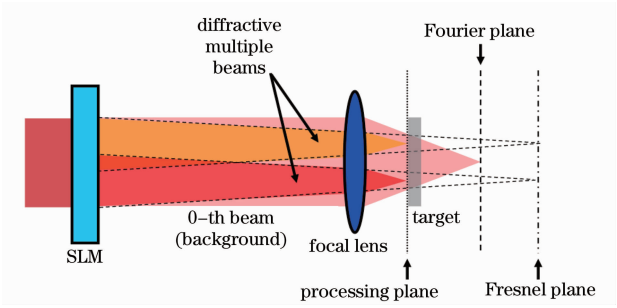

Fig. 8 Create multiple beams with the third type of hologram, which is the combination of the Fourier and Fresnel plane hologram

3 Calculation of CGHs

An optical beam can be represented by a complex field, which can be written as

$$\psi_0 = A\exp(\mathrm{i}\varphi_0), \tag{4}$$

where A is the amplitude of the field and φ is the phase. The phase holograms act as a transmission, t, mathematically expressed as the following equation, which therefore modifies only the phase of the beam:

$$\psi_t = \exp(\mathrm{i}\varphi_h). \tag{5}$$

When the beam given by Eq. (4) incidents on the SLM, the complex amplitude profile of the beam after the modulation of the phase hologram will be

$$\psi_h = \psi_0 \cdot \psi_t = A_0\exp[\mathrm{i}(\varphi_0 + \varphi_h)]. \tag{6}$$

The algorithms, which will be described in this section, are used to generate this phase pattern φ_h.

3.1 Algorithms for Calculating Fourier Plane Holograms

The Fourier plane phase hologram is designed such that when the modified beam, ψ_h, is focused by a lens, the light intensity distribution in the image space (at the focus of the lens) is the one desired, e. g., multiple focused spots at prescribed positions.

According to Fourier optics, there is a Fourier transform relationship between the complex field, ψ_h, in the pupil plane of the focal lens, onto which the plane of the SLM is imaged, and the complex field, ψ_i, at the focus of the lens in image space, which can be shown as

$$\psi_i(x_i, y_i) = FT\{\psi_h(x_h, y_h)\}. \tag{7}$$

The image space field can therefore be thought of as a scaled version of the far-field diffraction pattern that would be produced by the beam leaving the SLM. If one of ψ_h or ψ_i is known, it is straightforward to calculate the other unknown field by taking the forward or inverse Fourier transform of the known field, as shown in Fig. 9. The algorithms to be introduced in the following are the means of calculating the phase hologram for a desired far-field intensity pattern, e. g., a certain number of multiple beams with arbitrary geometry for multi-beam applications.

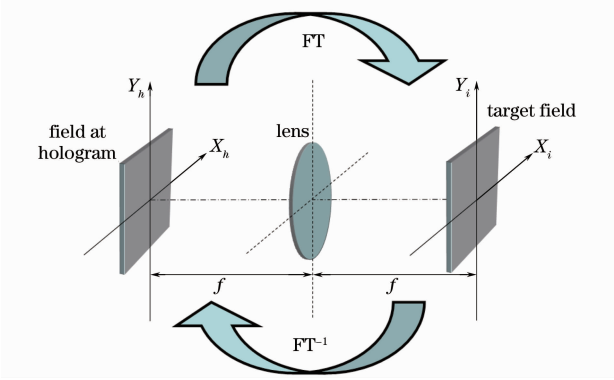

Fig. 9 Fourier relationship between the plane of the hologram and the image space of the focal lens

3.1.1 The GS Algorithm

As mentioned, with its wide applications from holographic optical tweezers to ultra-fast laser parallel micro-processing[32,50,69], the Fourier-transform-based the GS algorithm, first published by Gerchberg and Saxton in 1972[67], is one of the most popular methods to calculate Fourier plane CGHs.

The GS algorithm can be used to calculate the phase required in the hologram plane to produce a predefined intensity distribution in the focal plane of the lens. The target intensity distribution is defined in the image space as $I_t(x_i, y_i)$, and the aim is to find $\varphi_h(x_h, y_h)$ such that $(FT\{\exp(\mathrm{i}\varphi_h)\})^2 = I_t$. To find the desired phase φ_h, the algorithm starts at the hologram plane with a random φ_r and constant unit amplitude. Therefore, for the first iteration step, the light field in the hologram plane is

$$\psi_{h,1} = \exp(\mathrm{i}\varphi_r). \tag{8}$$

For the first and sub-sequent iteration, the light field is propagated to the image space by taking its Fourier transform, i. e., for the k-th iteration,

$$\psi_{i,k} = FT\{\psi_{h,k}\}. \tag{9}$$

Then, the light field in the image space is modified by keeping the phase but replacing the intensity with the target intensity, I_t:

$$\varphi_{i,k} = \arg(\psi_{i,k}), \tag{10}$$

$$\psi_{i,k}' = \sqrt{I_t}\exp(\mathrm{i}\varphi_{i,k}). \tag{11}$$

The resulting light field is then propagated back to the hologram plane by taking its inverse Fourier transform:

$$\psi_{h,k}' = FT^{-1}\{\psi_{i,k}'\}. \tag{12}$$

The iteration is finally completed by again keeping the phase but replacing the intensity with uniform constant intensity:

$$\varphi_{h,k+1} = \arg(\psi_{h,k}'), \tag{13}$$

$$\psi_{h,k+1} = \exp(\mathrm{i}\varphi_{h,k+1}). \tag{14}$$

Since the laser beam has a Gaussian intensity profile, it is sometimes desirable to replace the intensity with the Gaussian profile. With a few iterations, n, the algorithm converges such that the argument of the light field at the hologram plane is the phase required to produce the target field in the image space:

$$\varphi_{h,n} = \arg(\psi_{h,n}). \tag{15}$$

Figure 10 shows how to generate a phase hologram with the GS algorithm. The calculation starts from the upper left corner, and moving clockwise runs through the forward/inverse Fourier transforms with replacing intensity and keeping the phase, as in the iterative approach described above, and finally generates the phase hologram shown at the bottom left corner.

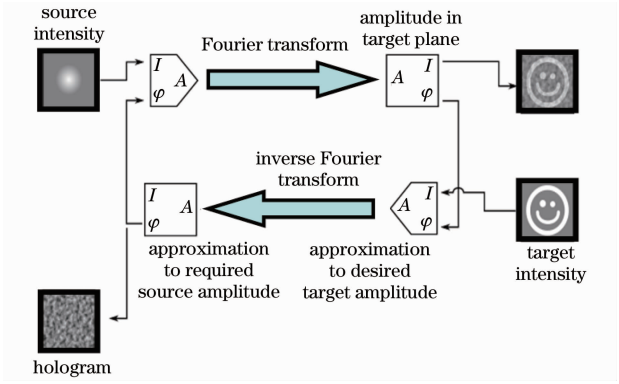

Fig. 10 Diagram showing how to generate a phase hologram with the GS algorithm

The GS algorithm can be used to generate not only multiple focussed spots of light but also arbitrary 2D intensity distributions. Extended by Haist *et al*.[70], the GS algorithm has been demonstrated to modulate the intensity distributions in several planes simultaneously. Later, Sinclair *et al*.[40] successfully applied this algorithm in holographic optical tweezers, simultaneously trapping several objects in individually controllable arbitrary 3D positions. In contrast to the simpler and computationally faster non-iterative algorithm, to be next introduced (the non-iterative complex superposition of prisms (and lenses for 3D patterns)[53,54], where the phase between each multiple beams is fixed), this algorithm takes advantage of the phase freedom and iteratively optimizes the focal-plane intensity distribution by varying both these phase values and φ_h.

3.1.2 The Non-iterative Complex Superposition of Prisms (and Lenses for 3D Patterns) Algorithm

First introduced by Liesenser *et al*.[54], the non-iterative complex superposition of prisms (and lenses for 3D patterns) algorithm is a simple and computational fast method to calculate phase CGHs for the generation of multiple beams.

As shown in Fig. 11, combining the phase of basic optical components, prisms or gratings, which result in lateral shifts, and lenses, which produce axial shifts in a similar way, the algorithm, sometimes called the gratings and lenses (GL) algorithm[53], can generate 3D arbitrary multi-beam pattern in the imaging space after a focal lens.

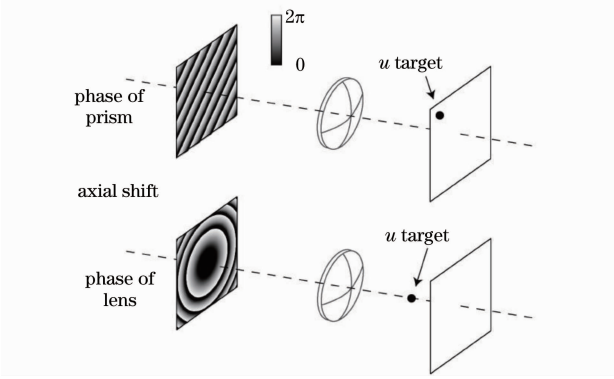

Fig. 11 Phase required for lateral and axial shifts, quoted from Leach *et al*.[53]

It is known that a single beam with planar phase fronts at the plane of the hologram, i. e., φ_h = constant, corresponds to a single focussed spot in the image space. If the hologram plane has an inclined phase front, the spot in the image space will be laterally displaced from the optic axis. This is equivalent to passing the light through a prism with a small angle that introduces a linearly increasing phase delay φ_{prism} across the beam. The phase at the hologram plane required to produce a lateral shift $(\Delta x, \Delta y)$ in the position of the focused spot is given by

$$\varphi_{\mathrm{prism}}(x_h, y_h) = \alpha(\Delta x x_h + \Delta y y_h), \tag{16}$$

where α is a coefficient that depends on the imaging

characteristics and wavelength.

To generate 2D arbitrary multi-beam pattern at the focal plane of the lens, the phase at the hologram plane, φ_h, should be the complex superposition of the prism phases, each of which shifts a focused spot onto one of the requested positions, $(\Delta x_i, \Delta y_i)$, as shown in Fig. 12. Accordingly, φ_h can be expressed as

$$\varphi_h = (\varphi_{\text{prism}-1} + \varphi_{\text{prism}-2} + \cdots \varphi_{\text{prism}-n}) \bmod 2\pi = \left(\sum_{i=1}^{n} \varphi_{\text{prism}-i}\right) \bmod 2\pi. \quad (17)$$

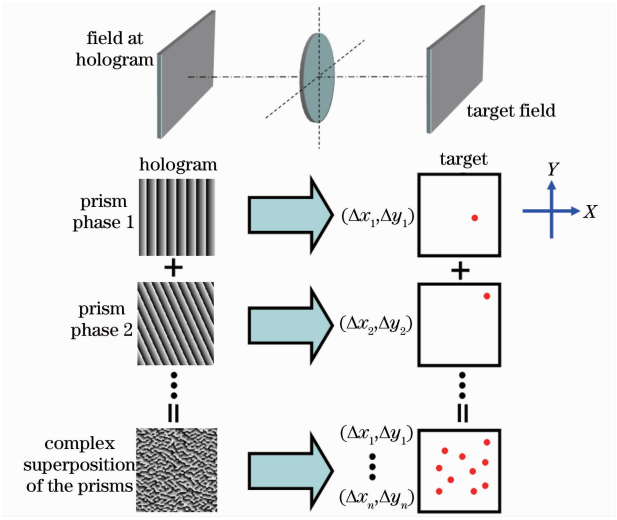

Fig. 12 2D arbitrary multi-beam pattern generated by complex superposition of prism phases

To also axially shift each of the focal spots in the image space, an additional lens phase should be added, hence obtaining multi-beam pattern in 3D. The lens phase can be given as

$$\bar{\omega}_{lens}(x_h, y_h) = -\frac{k}{2f}(x_h^2 + y_h^2), \quad (18)$$

where f is a function of the axial shift distance and $k = 2\pi/\lambda$ is the wave number of the light. This is equivalent to passing the light through an additional lens with focal length, f. With both prism and lens phase added, the focussed spots are displaced not only laterally but also axially, i. e., three-dimensionally. The phase of the beam at the hologram plane is required to be the (modulus 2π) sum of φ_{prism} and φ_{lens}

$$\varphi'_h = \left[\sum_{i=1}^{n} (\varphi_{\text{prism}-i} + \varphi_{\text{lens}-i})\right] \bmod 2\pi. \quad (19)$$

Clearly, without any iterative calculations required, the GL algorithm is simple and computationally fast. With a standard personal computer, the hologram calculation speed can meet the requirement of real time change in multi-beam pattern. The literature demonstrates dynamic CGHs calculation for 2D/3D trapping and manipulation the micro/nano-particles by optical tweezers with this algorithm[50,55,56].

However, the diffractive efficiency, η, the energy of light directed to the requested positions over the total input energy, and the uniformity of the diffracted multiple beams, may be low and poor, especially for the pattern with symmetric geometry, due to the high possibility that one or more ghosts overlap with the desired diffractive (+1) order beams, a process called 'degeneracy'[68]. In most cases, the ghosts are the higher order diffractive peaks produced by the phase gratings, i. e., the prism phases. As introduced, a phase grating, equivalent to a prism, deflects an enhanced +1 order beam to a required position $(\Delta x_i, \Delta y_i)$, by imposing an appropriate phase φ_{prism}; however, it also generates other diffractive orders (e. g., −1 order) with much lower intensity. For the GL algorithm, the phase between each multiple beams is fixed, without any freedom to avoid the ghosts overlapping with the desired diffractive +1 order, hence causing the high possibility of degeneracy.

Probably due to this high possibility of low diffractive efficiency and poor beam uniformity, the GL algorithm is not usually used to generate multiple beams for high precision ultra-fast laser processing. The current author may be the first to attempt parallel micro-processing by using ultra-fast lasers with diffractive multiple beams generated by the GL algorithm. With the considerations of spectral bandwidth of the laser source and the geometric pattern design of multiple beams, the results shown and discussed in chapter three and four, have also demonstrated high diffractive efficiency and excellent beam uniformity, compared with those produced by the time-consuming GS iterative algorithm.

3.2 The Multiplexing Phase Fresnel Lenses Algorithm for Calculating Fresnel Plane Holograms

The use of the multiplexing phase Fresnel lenses (MPFL) algorithm to calculate Fresnel plane holograms, was first attempted by Hasegawa *et al.*[33,35] to generate multiple beams for parallel femto-second laser processing.

The complex amplitude of a phase Fresnel lens

(PFL) is

$$\psi_{\mathrm{PFL}}(x,y) = \exp\left(\mathrm{i}k\frac{(x-x_i)^2+(y-y_i)^2}{2z_i}\right), \quad (20)$$

where z_i is a focal length and $k = 2\pi/\lambda$ is the wave number. With PFL, the light can be focussed at (x_i, y_i, z_i) in the Fresnel diffraction field. Accordingly, the MPFL which can generate n multiple foci, three-dimensionally arranged in the Fresnel diffraction field, is expressed as

$$\psi_{\mathrm{h-MPFL}}(x,y) = \sum_i^n \exp\left(\mathrm{i}k\frac{(x-x_i)^2+(y-y_i)^2}{2z_i}+\mathrm{i}\varphi_i\right), \quad (21)$$

where the amplitude is set to 1 and φ_i is the centre phase. The diffraction peaks are made uniform by changing the centre phase and size of each PFLs while taking account of the intensity distribution of the irradiated laser pulse and the spatial frequency response of the SLM[33].

With the phase hologram calculated by the MPFL algorithm, 2D and 3D parallel femto-second laser processing with single-pulse irradiation has been demonstrated[33,35]. This may be useful to fabricate micros-tructure inside a material and on an arbitrary-shaped material surface. However, the parallel processing with diffractive multiple beams reconstructed at the Fresnel plane might not work well for large area surface micro-structuring applications due to the small diffraction angle allowing only a small area to be fabricated.

4 Methods to Remove Zero Order Beam

Since the diffractive efficiency η (defined as the percentage of the total energy output divided by the energy diffracted to the desired orders) cannot reach 100% with the current commercial SLMs, there is always part of output energy un-diffracted, which is called the zero order beam. To generate a diffractive pattern with over 10 desired multiple beams, η is measured at approximately 50%, meaning that the zero order beam, contains about half of the output energy and is always much stronger than any of the desired orders, as shown in Fig. 13. Therefore, the zero order beam may lead to unwanted damage on the sample during processing and hence should be removed.

4.1 Removal of the Zero Order with a 4*f* Optical System

To physically block the zero order beam at the Fourier plane of a 4*f* optical system might be the most common and direct method to avoid sample damage by the focussed zero order beam. This method is shown in Fig. 14, in which lenses 1 and 2, both having a focal length of f, form a 4f optical system, i.e., AB = BP = PC = CD = f. The input beam, represented by a complex field, $\psi_0 = A\exp(\mathrm{i}\varphi_0)$, is modulated by the phase hologram, $\psi_t = \exp(\mathrm{i}\varphi_h)$, displayed on the SLM. Therefore, after reflection, the modulated beam, $\psi_h = \psi_0 \cdot \psi_t = A_m\exp[\mathrm{i}(\varphi_0+\varphi_h)]$, is diffracted with an angle θ to the desired position, while the zero order beam, $\psi_0 = A_0\exp(\mathrm{i}\varphi_0)$, is not diffracted, i.e., $\theta = 0$, and hence is separated from the desired orders at the Fourier plane P through lens 1. Since a small target is put at Q to only block the zero order beam, the optical field at A is reconstructed after lens 2 at D, but without the un-modulated zero order beam. As a scanning galvanometer with a flat field f-θ lens

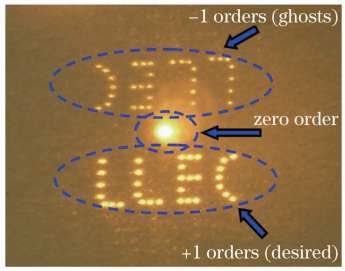

Fig. 13 An 'LLEC' pattern with 32 desired diffractive beams projected on a paper screen. The brighter spot in the middle, corresponds to the zero order beam, and is much stronger than any of the desired spots, +1 orders at the bottom. The upper weaker spots are the −1 orders, the undesired higher orders sometimes called 'ghosts', which are kept below the material ablation threshold and have no effect on the sample. LLEC stands for Lairside Laser Engineering Centre, where the laboratory of the present research is located

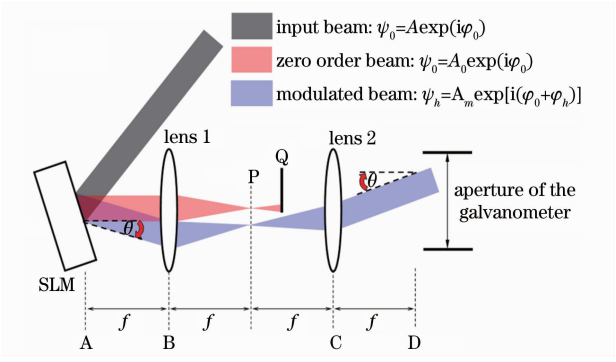

Fig. 14 Schematic diagram for blocking the zero order beam at the Fourier plane P of the 4f optical system[41]

working as a focal system is used in the current research to make parallel processing more flexible, the modulated beam will go through the galvanometer aperture and will be again focussed on the sample to allow material machining.

4.2 Removal of the Zero Order by Adding a Fresnel Zone Lens

Alternatively, in the current research, the zero order beam was also significantly defocused at the processing plane by adding PFL onto the CGH. The focal length (f_1) of the PFL can be adjusted by the software developed by Holoeye[44], as shown in Fig. 15. Only the diffracted beams were converged ($f_1>0$) or diverged ($f_1<0$) by the PFL while the zero order beam was unaffected, hence separating the focal planes of the diffracted beam from the zero order beam, as shown in Fig. 16. The following beam matrix equation describes the propagation of the diffracted beam from the liquid crystal on silicon (LCoS) surface (A) to its focal plane (B)

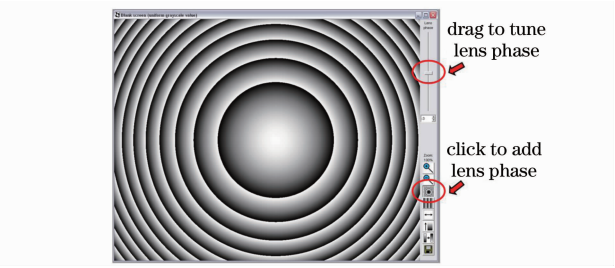

Fig. 15 Interface of the software developed by Holoeye[44], which can easily superimpose and adjust the phase of the PFL[42]

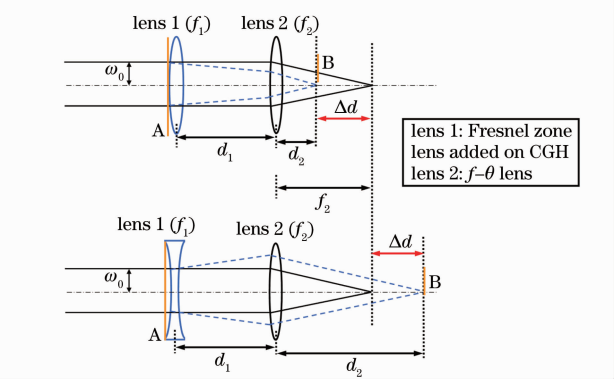

Fig. 16 Schematic showing the method to separate the focal plane of diffracted beams from the zero order beam. The added PFL, lens 1, can work as either a positive lens (upper) or a negative lens (lower) to obtain the separation, Δd. The beam matrix equation below describes the propagation of diffracted beam from LCoS surface (A) to its focal plane (B)[42]

$$\begin{pmatrix} X_B \\ \mathrm{tg}\theta_B \end{pmatrix} = \begin{pmatrix} 1 & d_2 \\ 0 & 1 \end{pmatrix} \times \begin{bmatrix} 1 & 0 \\ -\dfrac{1}{f_2} & 1 \end{bmatrix} \times \begin{pmatrix} 1 & d_1 \\ 0 & 1 \end{pmatrix} \times \begin{bmatrix} 1 & 0 \\ -\dfrac{1}{f_1} & 1 \end{bmatrix} \times \begin{pmatrix} X_A \\ \mathrm{tg}\theta_A \end{pmatrix}, \quad (22)$$

where X_A and X_B are the distances of the beam from the axis, and $\mathrm{tg}\theta_A$ and $\mathrm{tg}\theta_B$ are the gradients of the beam with respect to the axis at the position A and B, respectively. Since $\mathrm{tg}\theta_B = 0$ and $X_A = 0$, the focal plane separation (Δd) can be calculated by the following equation derived from the beam matrix equation

$$\Delta d = |d_2 - f_2| = \left| \frac{f_1 f_2 - f_2 d_1}{f_1 + f_2 - d_1} - f_2 \right|, \quad (23)$$

where $d_1 \approx 200$ mm was the distance between LCoS and f-θ lens, and $f_2 \approx 100$ mm was the focal length of f-θ lens. Thus

$$\Delta d = \left| \frac{100 f_1 - 20000}{80 + f_1} - 100 \right|. \quad (24)$$

A slightly defocused zero order beam can still damage the sample because it contains approximately 50% of the input pulse energy which was much stronger than any of the diffracted orders. Accordingly, f_1 must be adjusted carefully to allow sufficient Δd so that the fluence at the substrate is below the damage threshold. Figure 17 demonstrates a CGH calculated by the GL algorithm[53,54] to generate eight first order identical beams and its computational reconstruction, and Fig. 18 shows the micro-machined results on Ti6Al4V using the CGHs which were superimposed by PFLs with different f_1 to adjust Δd. Figure 18 shows that the defocused zero order beam still damaged the sample when the separation was $\Delta d = 1$ mm (middle lower picture), while it was totally removed when $\Delta d = 5$ mm (right lower picture).

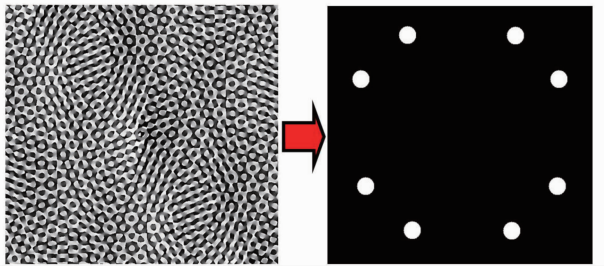

Fig. 17 A CGH calculated by the GL algorithm to generate eight first order identical beams (left) and its computational reconstruction (right)[42]

By superimposing a PFL, the desired diffractive multiple beams were focused on neither the

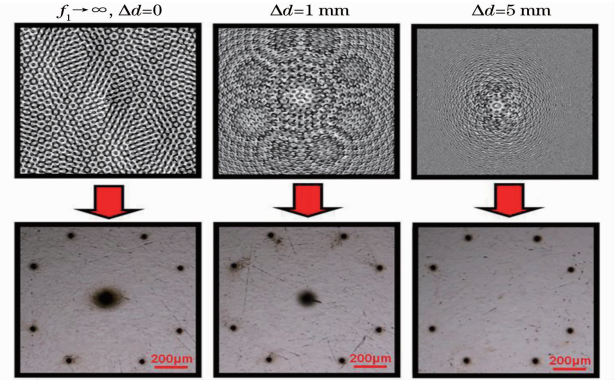

Fig. 18 CGHs superimposed by PFLs with different f_1 to adjust Δd (upper) and the machined results on Ti6Al4V (lower)[42]

Fourier plane nor the Fresnel plane and according to section 2.2, the CGH hence became the third type, the combination of the Fourier and Fresnel plane holograms.

5 Diffractive Multi-beam Ultra-fast Laser Surface Structuring

5.1 Experimental Setup

Figure 19 shows the schematic of the experimental setup with the $4f$ optical system, where a Clark-MXR CPA2010 laser system was employed, generating ultra-short laser pulses, at a pulse duration of 180 fs, a wavelength of 775 nm, and a repetition rate of 1 kHz which were attenuated by a half wave-plate and a Glan laser polarizer. After reflection on mirrors 1 and 2, the laser illuminated a reflective SLM LCoS device with 1024 × 768 pixels (Holoeye LC-2500), oriented at $< 10^\circ$ angle of incidence. A beam expanding telescope, with magnification of $M \approx 2$, was used to reduce the average intensity on the SLM, where the CGHs were displayed. The input optical beam was represented by a complex field, $\psi_0 = A\exp(i\varphi_0)$, and the SLM displayed a phase hologram, $\psi_t = \exp(i\varphi_h)$. Accordingly, after reflecting on the SLM (at A in Fig. 19), the beam was modulated to be $\psi_h = \psi_0 \cdot \psi_t = A_m \exp[i(\varphi_0 + \varphi_h)]$. Lenses 1 and 2 were two BK7 plano-convex lenses with anti-reflection coating. Referring to Fig. 19, since distance AB = BP = PM + MC = CN + ND $\approx f$ ($\approx$300 mm), a $4f$ optical system with unity magnification was formed. Accordingly, at D, the complex field was identical with that at A. The zero order reflected beam was spatially separated and blocked at Q. Just after D, the modulated beam, u_h, entered the 10-mm aperture of a scanning galvanometer system with a flat field lens (f = 100 mm). The proximity of the beam, u_h, (at D) to the input aperture of the galvanometer ensured that diffracted beams where transmitted cleanly to the substrate surface, while the flat field of the f-θ lens produced a near perfect focusing system. Substrates were mounted on a precision 4-axis (x, y, z, u) motion control system (Aerotech), allowing accurate positioning of the substrate surface at the laser focus.

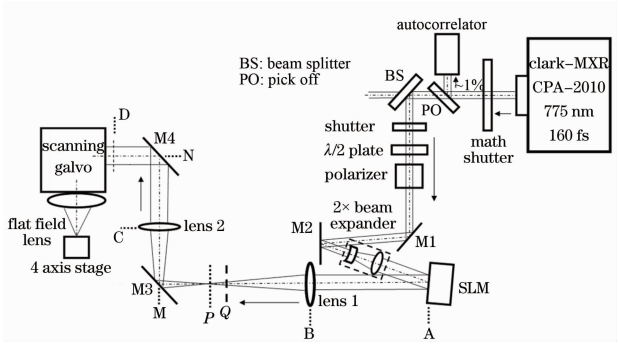

Fig. 19 Schematic of the experimental setup for the Clark-MXR CPA2010 laser with a $4f$ optical system

5.2 Static CGH Multi-beam Micro-processing

5.2.1 Precision Micro-drilling Using Diffractive μJ-level E_p Multiple Beams

Figure 20 shows optical micro-graphs of the surface structuring on silicon with an 'LLEC' pattern comprising 32 blind holes while Fig. 21 demonstrates a random spot pattern comprising 30 holes. Each hole pattern was micro-machined simultaneously on a silicon wafer by applying the calculated CGHs to create the desired geometries. The GL algorithm[43, 44], which is simple and computationally fast, was used to calculate CGHs producing multiple independent diffractive + 1 order beams for processing. The incident pulse energy on the SLM was $E_P \sim 300$ μJ. All diffractive spots had similar dimensions, indicating accurate calculation of the CGH. The large hole above the main pattern of the holes was generated by the zero order beam. The total input pulse energy was ~ 300 μJ, measured before the aperture of the scanning galvanometer. The energy diffracted into each of the desired

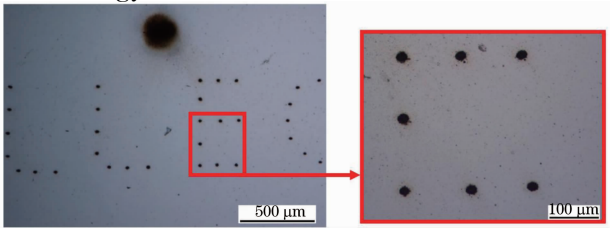

Fig. 20 'LLEC' pattern comprising 32 micro-sized holes[40]

beams was ~ 5 μJ.

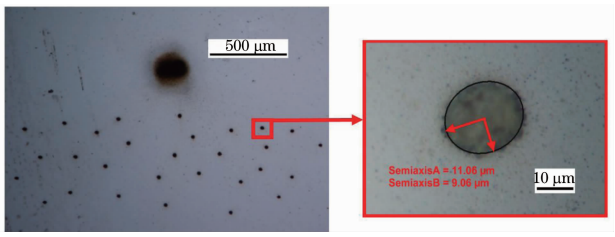

Fig. 21 Random spots pattern comprising 30 micro-sized holes[40]

The measured hole size versus distance from the zero order hole in both 'LLEC' and random spots patterns is shown in Fig. 22. The uniformity of the diffracted beams is shown by the measurements of the ablated spot diameters using a Wyko NT1100 optical surface profiler: $\Phi_1 = 20.3 \pm 1.2$ μm ('LLEC' pattern) and $\Phi_2 = 21.7 \pm 1.1$ μm (random spots pattern). To avoid large variations in the required intensity distributions between spots, it is advantageous to avoid patterns with a high degree of symmetry[40].

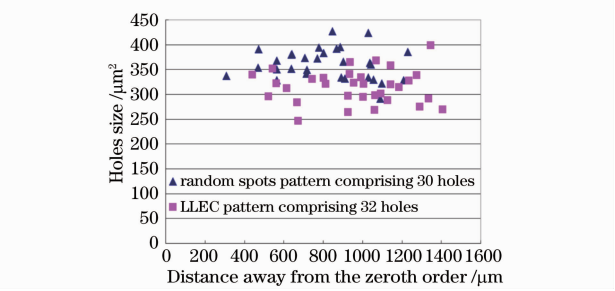

Fig. 22 Hole size versus the distance from each diffracted spot to the zero order hole in both 'LLEC' and random spots patterns[40]

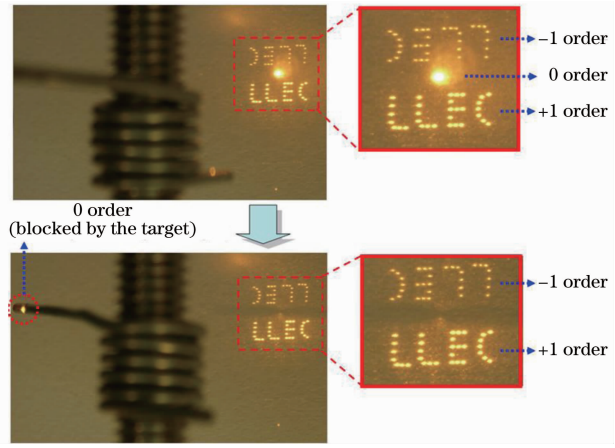

Fig. 23 Demonstration of the enhancement of the +1 diffracted orders (LLEC pattern) combined with blocking the zero order beam using a small metallic target. The image shows intensity distribution on a paper screen taken with a digital camera[41]

The un-diffracted zero order beam containing approximately 50% of the input pulse energy was blocked by a metallic target at position Q (Fig. 14). Referring to Fig. 23, digital camera images show the holographically produced energy distribution of the 'LLEC' pattern on a paper screen near the Fourier plane. The +1 order beams contain the majority of the diffractive energy because the CGH was designed to enhance them, while −1 order beams with much lower energy (≪material's ablation threshold) leave the substrate unaffected. The bottom two pictures of Fig. 24 demonstrate the absence of large holes, showing that the zero order beam was successfully removed.

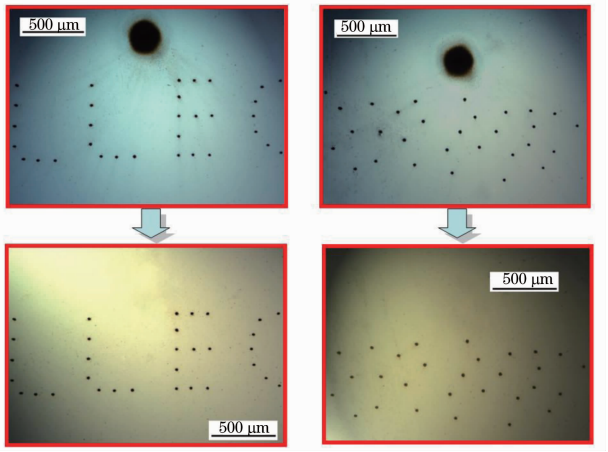

Fig. 24 Zero order beam removed when micro-structuring a silicon substrate with the 'LLEC' and random spots patterns[41]

5.2.2 Distortion of Beam Shape Caused by Finite Spectral Bandwidth

5.2.2.1 Observation of Distorted Beam Shape

A significant increase in eccentricity of hole shape was observed when applying a larger diffraction angle, which was probably due to the lateral chromatic aberration caused by the finite bandwidth ($\Delta\lambda$) of the laser source. If the input beam has a single wavelength, it will keep the initial round shape after the diffraction, as shown in Fig. 25(a). However, the laser beam, generated by Clark-MXR CPA2010 laser system, had a broad bandwidth, $\Delta\lambda \approx 5$ nm. Since the diffraction angle is proportional to the input wavelength, the components with longer wavelength will have a large diffraction angle, while the short wavelength components will be diffracted at a shorter angle, hence elongating the beam shape after the diffraction, as shown in Fig. 25(b).

To further investigate this phenomenon, the

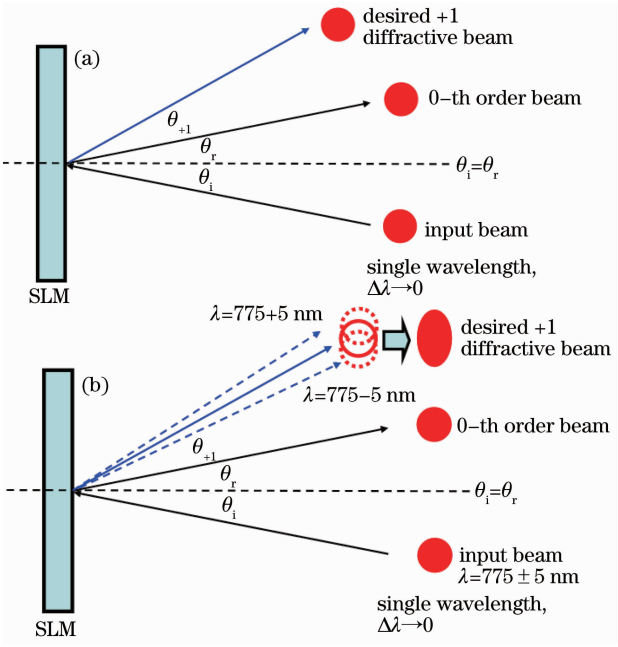

Fig. 25 Schematics showing that (a) the desired +1 diffractive beam keeps the around shape when the input beam has a single wavelength, i.e., $\Delta\lambda\rightarrow0$ and (b) the shape of desired +1 diffractive beam is elongated when the input beam has a broad bandwidth, $\Delta\lambda\approx5$ nm

holes were fabricated on silicon by the +1 order beams with varying diffraction angle. The results in Fig. 26 demonstrate that the eccentricity of the beam shape rises by increasing a diffraction angle and the long axis of the elliptically fabricated structure is aligned to the direction toward the zero order beam.

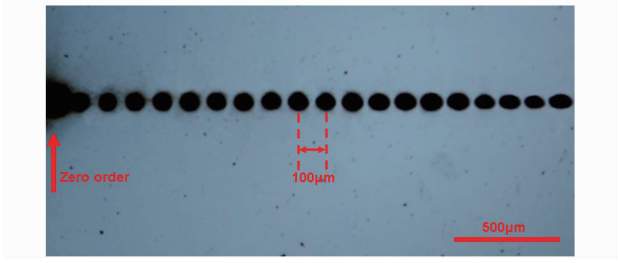

Fig. 26 Holes fabricated on a silicon sample by the +1 order beams with varying the diffraction angles. The larger hole on the left end was machined by the zero order, and all the other holes were generated by +1 orders with 0.057° diffraction angle increment from left to right[41]

5.2.2.2 Prediction of the Eccentricity of Beam Shape

The bandwidth limitation, mentioned above, is a characteristic of all diffractive optics when used with a broadband source (in this case, $\Delta\lambda\sim5$ nm). Based on the grating equation, $\Lambda(\sin\theta_m+\sin\theta_i)=m\lambda$, where Λ is the grating period and m is the order of diffraction, the expected variation of eccentricity e versus diffraction angle can be used to predict the drilled hole shape. Here, the incident angle θ_i on the SLM is $<10^\circ$, and the +1 order ($m=1$) diffraction angle θ_{+1} is $<2^\circ$; hence $\sin\theta_{+1}\sim\theta_{+1}$. The grating equation can be simplified to: $\theta_{+1}\approx\sin\theta_{+1}=\lambda/\Lambda$, where Λ is the grating period. Hence by differentiating, the following is obtained:

$$\frac{\Delta\theta_{+1}}{\Delta\lambda}=\frac{1}{\Lambda},\ \text{or}\ \Delta\theta_{+1}=\frac{\Delta\lambda}{\Lambda}. \tag{25}$$

If f is the focal length of the f-θ lens, the elongation Δl caused by $\Delta\lambda$ at the focal plane is then

$$\Delta l=f\cdot\Delta\theta_{+1}=\frac{f}{\Lambda}\Delta\lambda, \tag{26}$$

while the diameter of the focused spot can be calculated by

$$2\omega_0=\frac{4M^2f\lambda}{\pi D}, \tag{27}$$

where D is the raw beam (spot) diameter and $M^2\sim1$ is the beam quality factor. Thus, the eccentricity e at a given diffraction angle can be calculated by $e=a/b\approx(\Delta l+2\omega_0)/(2\omega_0)$, where a and b are the major and minor semiaxis of the elliptical hole shape. The graph shown in Fig. 27 indicates excellent agreement between the experimental and calculated eccentricity, e, which increases linearly when varying the diffraction angle.

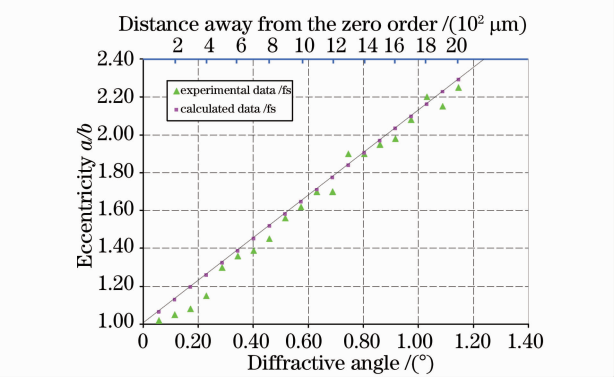

Fig. 27 Experimental and calculated eccentricity a/b of machined holes versus diffraction angle showing, excellent agreement. Eccentricity increases linearly with diffraction angle[41]

5.2.2.3 Stability of Processing Affected by the Distorted Beam Shape

The distorted intensity profile at higher angles of diffraction also affects ablation. Figure 28 shows a comparison of measured ablation depth on Ti6Al4V with diffraction angle and pulse number. In each case, pulse energy was $E_p\sim5$ μJ and the

ablation depth decreased with increasing diffraction angle due to the growing ellipticity of beam shape. Accordingly, to ensure precision femto-second processing with a 5-nm bandwidth (at $\lambda = 775$ nm), the diffraction angle should be limited to $\theta_1 < 0.5°$ where the eccentricity $e = a/b < 1.5$.

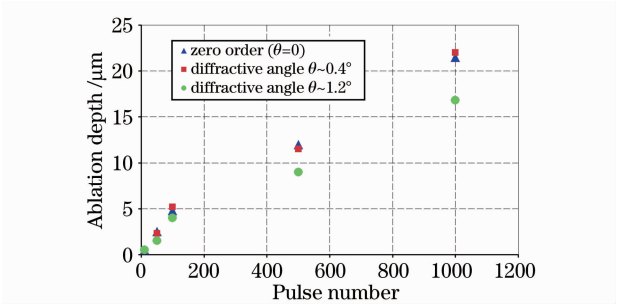

Fig. 28 A comparison of ablation depth on Ti6Al4V with diffraction angle and pulse number, showing that the ablation depth drops at higher angles due to increasing distortion of the intensity profile[41]

5.3 Dynamic Diffractive Pattern Micro-processing

While static holograms are useful and can be combined with the galvanometer system to demonstrate parallel processing with fixed spot geometry, processing by real time controlling the CGHs is demonstrated in this section.

5.3.1 Response Time of SLM

When addressing a series of CGHs in real time, the refresh rate (i.e., the number of CGHs displayed per second) is significantly restricted by the response time, which is a period of time required to fade out the previous CGH (fall time) and build up a new one (rise time). In this section, the response time of the Holoeye LC-R 2500 is investigated.

In the experiment, two CGHs, calculated by the GL algorithm, capable of generating three desired diffractive beams individually, were alternately displayed on the SLM at a 10-Hz refresh rate, whilst the laser was scanned in a straight line at a speed of 50 mm/s on a polished silicon sample by the scanning galvanometer. Fig. 29 shows an optical micrograph of the machined pattern on the silicon sample, where CGH1 was fading out and CGH2 was building up during the scanning. Due to the quick scanning speed, partially or completely separated single-pulse-machined craters (holes) were produced on the surface of the sample. Since the pulse repetition rate was 1 kHz, the period of time between two adjacent holes was 1 ms. On the left hand side of Fig. 29, towards the scanning direction, the size of the holes machined by the diffractive order beams decreases, while, contrarily, the zero order machined holes increase in size. This indicates the fading out of the CGH1, where the diffracted pulsed energy was gradually transferred back to the zero order beam. Similarly, the increase of the diffractive beam hole size and the decrease of the zero order beam hole size on the right hand side Fig. 29 represent the time period when CGH2 was gradually building up and the pulse energy was re-diffracted to the desired multiple beams.

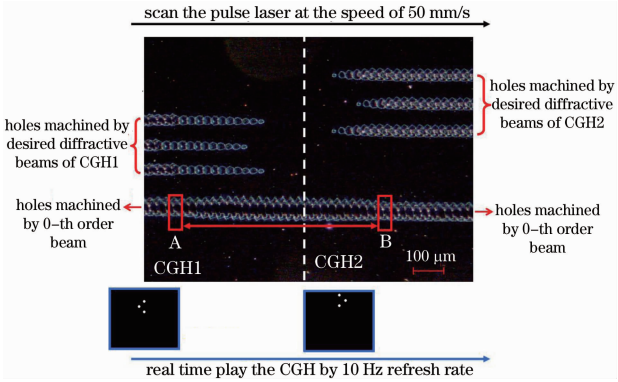

Fig. 29 Optical micrograph of the machined pattern on a silicon wafer, where CGH1 was fading out and CGH2 was building up during the scanning. The number of zero order beam machined holes between A and B was 27, and the period of time between two adjacent holes was 1 ms; hence the respose time was estimated at ~27 ms

As shown in Fig. 29, by counting the number of order machined craters from A with CGH1 starting to fade out, to B, with CGH2 built up completely, the response time was estimated at ~27 ms (fall time ~17 ms, rise time ~10 ms), which matches reasonably the value given by the manual of the Holoeye LC-R 2500, 28 ms (fall time ~18 ms, rise time ~10 ms), shown in Fig. 30. Accordingly, restricted by the response time, the maximum CGH playing rate should be less than 50 Hz. However, if

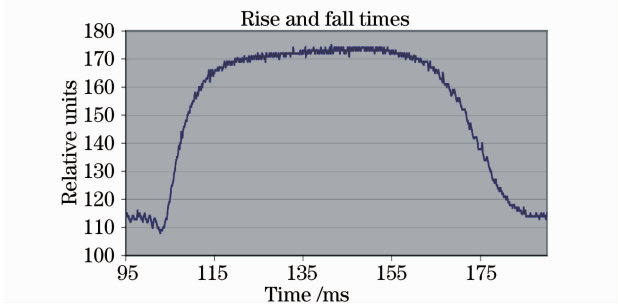

Fig. 30 Rise and fall times of SLM (LC-R 2500) given by Holoeye[48]

there is a little change in the position of the desired diffractive beams when building up the successive CGH, 50-Hz rate of CGH playing also allows perfectly good machining results in parallel processing.

5.3.2 Micro-processing by Real time Playing CGHs

Figure 31 shows a pattern comprising 121 holes completed by real time playing of 15 stored CGHs at 20-Hz refresh rate, and Fig. 32 demonstrates the formation of the pattern, which was completed within 0.75 s. The incident pulse energy on the SLM was $E_P \sim 300\ \mu J$.

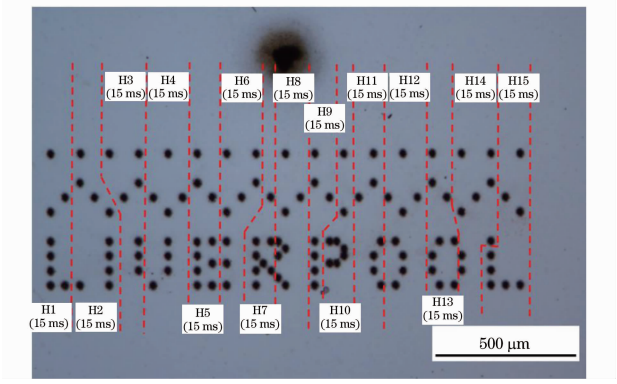

Fig. 31 Pattern completed by real time playing 15 series of CGHs at 20-Hz refresh rate (50 ms duration per CGH)[40]

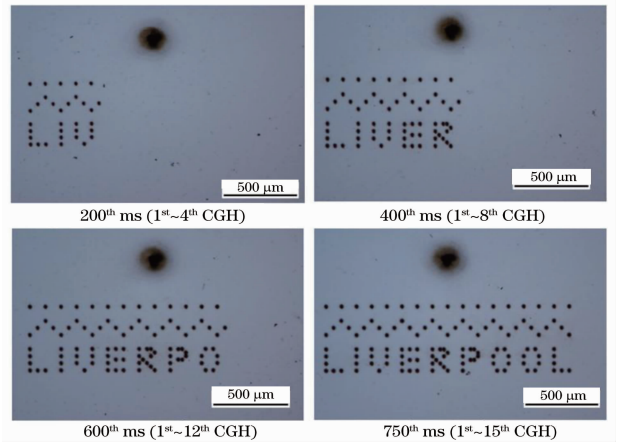

Fig. 32 The formation of the pattern[40]

Combining real time control of the CGHs with scanning, diffractive multi-beam processing has significant potential to produce complex surface micro-machining patterns. Figure 33 illustrates this on a polished Ti6Al4V substrate where six micro-channels a~f were generated by applying the appropriate CGHs at 50-Hz refresh rate while simultaneously scanning the diffracted spots at a speed of 1mm/s. The resulting micro-channels a~f, were ~ 40-μm wide and ~ 10-μm deep. The large channel above, was machined by the zero order beam.

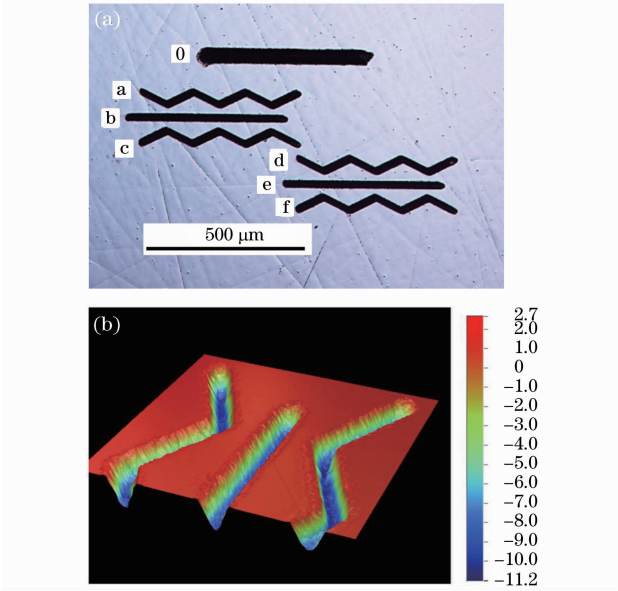

Fig. 33 Micro-channels obtained by combining CGH real time control with galvanometer scanning[40]. (a) whole pattern view (5 × objective); six channels a ~ *f* were generated by the diffractive beams while the wider channel 0 above was formed by zero order beam; (b) 3D zoom view by Wyko NT1100 optical surface profiler, where ~10 μm depth (10 times over scan) micro-channels are illustrated

5.3.3 Synchronizing the Action of Hologram Application with Scanning Techniques

By synchronisation of real time playing holograms with scanning, 2D surface micro-structuring on Ti6Al4V was demonstrated. A pattern 'OPTICS' (in Chinese and English) comprising 129 holes processed on a Ti6Al4V substrate using 7 CGHs combined with the galvanometer scanner is shown in Fig. 34, while Fig. 35 shows the pattern with zero order removed. Incident pulse energy on the SLM E_p is ~150 μJ, the measured hole diameter $\Phi \sim 25\ \mu$m, and depth ~2.3 μm corresponding to an exposure time

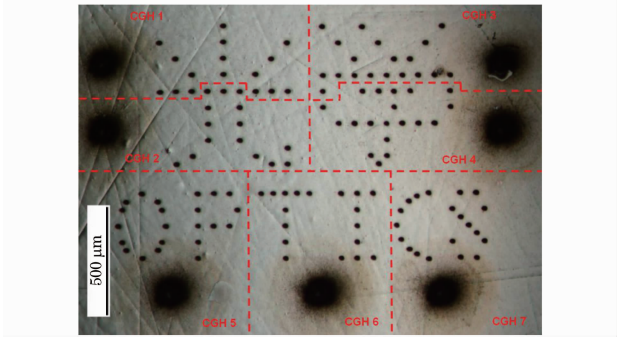

Fig. 34 'OPTICS' pattern with zero order holes, completed by 7 CGHs applied at appropriate positions using the galvanometer scanner[41]

of 200 ms (i.e., 200 pulses), with pulse energy $E_p \sim 5$ μJ in each +1 diffracted order beam. As each CGH generated more than 15 higher order holes simultaneously, a throughput gain factor $G > 15$ was demonstrated compared to single beam processing in this case.

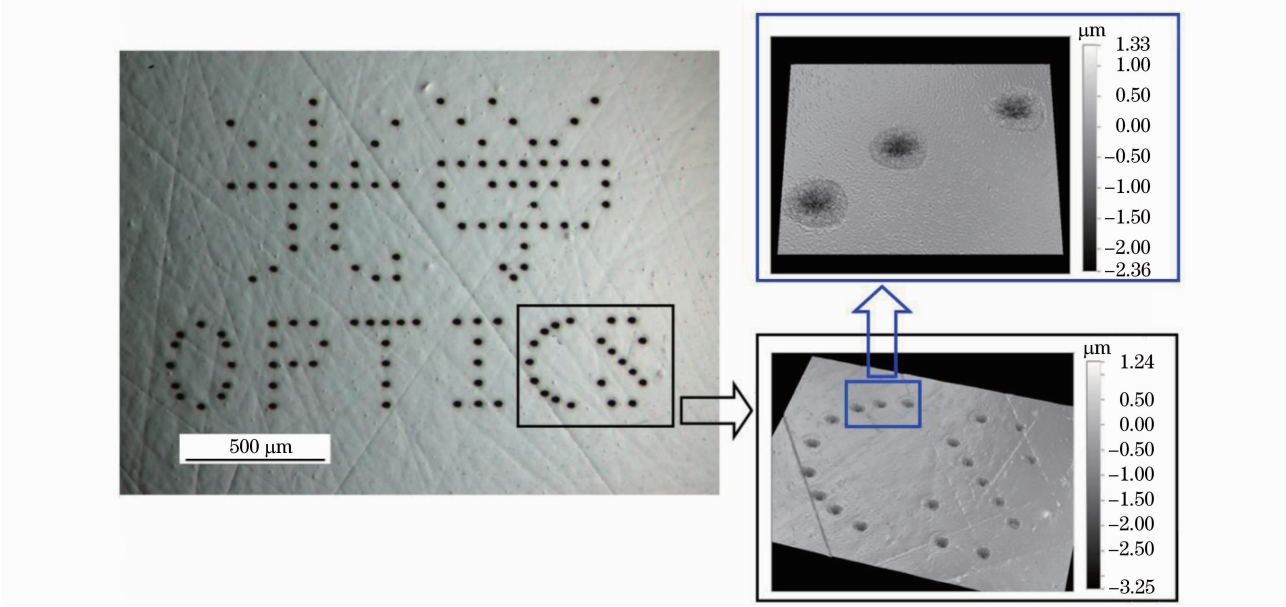

Fig. 35 'OPTICS' pattern with zero order holes eliminated (The insert 3D pictures were measured using Wyko NT1100 optical surface profiler, illustrating the depth of the holes)[41]

As samples chosen for this research, both silicon wafer, a significant semiconductor widely used in the fabrication of integrated circuit and other micro devices, and Ti6Al4V, a metallic alloy extensively used in aerospace and bioscience, have a relatively low threshold for femto-second pulse induced ablation. Thus, when using single beam to machine, extensive attenuation may required to provide low pulse energy, i.e., just above the threshold, hence resulting in low processing efficiency. Here, the above results from parallel processing demonstrated great advantages in term of increasing both processing throughput and efficiency.

5.4 Diffractive Multi-beam Surface Micro-processing Using 10-ps Laser Pulse

A pico-second laser system (High-Q IC-355-800 nm) with much narrower spectral bandwidth ($\tau \approx 10$ ps, $\Delta\lambda \approx 0.1$ nm) was employed for diffractive multi-beam processing. Compact solid-state pico-second laser systems ($\tau < 15$ ps) with high pulse energy, high average power and high repetition rate, have advantages over femto-second systems for high precision micro-machining[7, 8]. The experimental set-up was similar to that shown in Fig. 19. Dielectric coated SLM, Hamamatsu X10468, was used. Table 1 shows the specifications of the X10468 in comparison with that of Holoeye LC-R2500. It is worth noting that the X10468 has a dielectric mirror, which provides 95% light utilization efficiency, but can only work within a specified wavelength range. By comparison, the LC-R2500 is equipped with a metallic coated mirror that offers lower light utilization efficiency ~75%, but covers a wider wavelength range from visible to near-infrared (NIR). Applying a voltage to the X10468, which is a parallel-aligned nematic crystal device, results in the LC molecules aligning horizontally along the optical axis, hence causing a phase change to the light polarized along the molecular axis, but leaving the light polarized perpendicular to the molecular axis completely unaffected. Compared with the parallel aligned nematic crystal device, the LC-R2500 has a 45° twisted nematic LC layer in which the LC molecules are arranged in a twisted array from the front to the back. This kind of device can not only modulate the phase of light, but also rotate the plane of polarization.

Table 1 Specifications of the SLMs[45, 48]

Model	Hamamatsu X10468-04	Holoeye LC-R2500
LC Type	Parallel-aligned nematic	45° twisted nematic
Mode	Phase only	Phase & Amplitude
Resolution (pixels)	SVGA(800×600)	XGA(1024×768)
Pixel Pitch (μm)	20	19
Effective area (mm^2)	16×12	19.5×14.6
Mirror coating	Dielectric	Broadband metallic
Readout wavelength (nm)	510±50	400～1064
Reflectivity	95%	～75%*
Fill Factor	95%	93%
Response Time** (rise/fall ms)	15/30	10/18
Frame Rate (Hz)	60	72

* The actual reflectivity depends on readout light wavelength.

** Time required to change from 10 % to 90 % for 2π modulation.

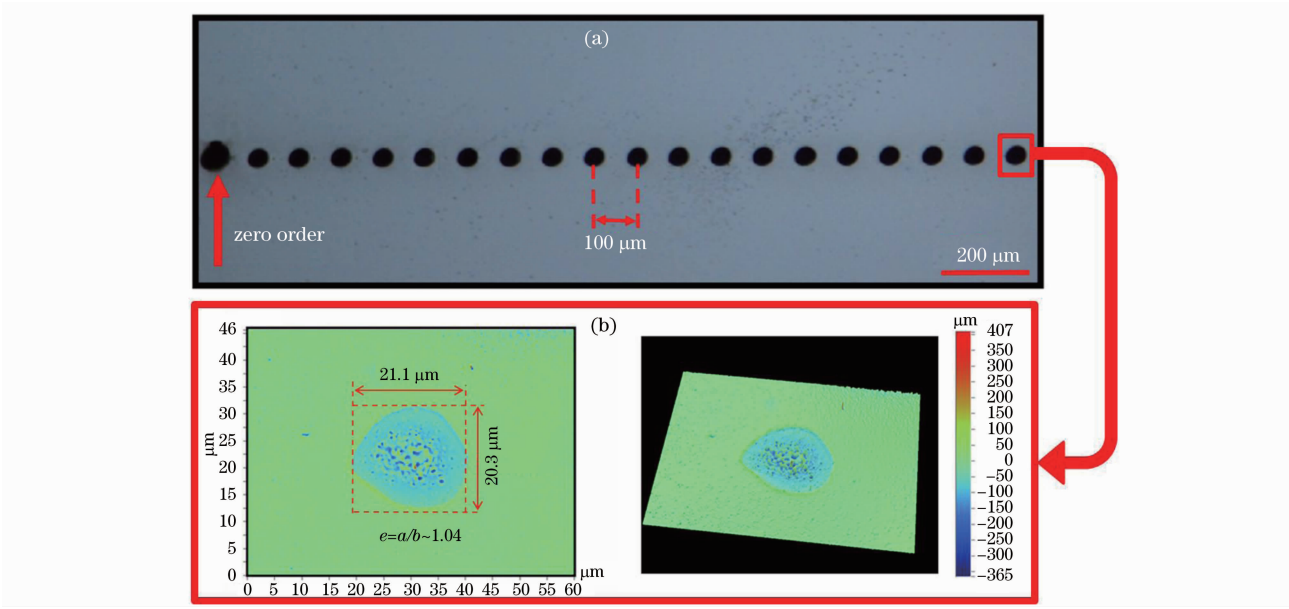

Fig. 36 (a) A series of holes drilled on a silicon sample when varying the diffraction angle; (b) The 2D (left) and 3D (right) micrographs with large magnification, showing the shape of the hole, fabricated by single 10-ps pulse, when applying large diffraction angle, $\theta > 1°$[42]

5.4.1 Spectral Bandwidth Effect on Diffracted Beam Shape

Figure 36 (a) demonstrates a series of holes drilled on a silicon sample using 10-ps ($\lambda_0 \approx 1064$ nm, $\Delta\lambda \approx 0.1$ nm) pulses with varying diffraction angle, while, in Fig. 36(b), the 2D (left) and 3D (right) micrographs with large magnification clearly shows the reasonably round hole shape when applying a large diffraction angle ($\theta > 1°$). The eccentricity $e = a/b$ of these drilled hole shapes as a function of diffraction angle is plotted in Fig. 37, and shows that e increases only very modestly, $e < 1.04$. Figure 38 shows that there is a negligible variation of ablation depth (1000 pulses, $E_p \approx 5$ μJ) with increasing diffraction angle, demonstrating a high degree of reproducibility of diffractive multi-beam processing. The above results indicate that the elongation of diffracted beam shape caused by

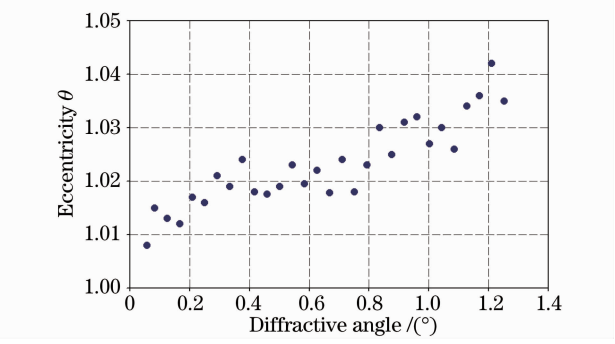

Fig. 37 The eccentricity e of hole shape drilled by 10-ps when varying the diffraction angle[42]

chromatic distortion can be eliminated by employing pico-second laser pulses ($\tau \approx 10$ ps) with narrower bandwidth, hence allowing constant ablation rate.

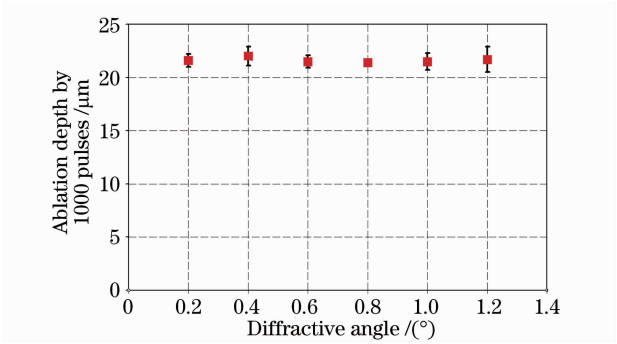

Fig. 38 Variation of ablation depth using one thousand 10-ps pulses ($E_p \approx 5$ μJ) when varying the diffraction angle[42]

5.4.2 High Power Parallel Processing with High Repetition Rate at $f = 20$ kHz

With the pico-second system ($\tau \approx 10$ ps) operating at high repetition rate ($f = 20$ kHz) and maximum output ($P_{average} \sim 2.5$ W), parallel processing was demonstrated, using a 25 diffractive beams pattern, created by a CGH calculated by the 2D GS algorithm. The schematic given in Fig. 39 demonstrates the design of the beams pattern and the method of scanning, while the micrographs in Fig. 40 show the micro-machining results on a polished Ti6Al4V sample. A 10 mm × 10 mm area covered by ~ 2-μm deep micro-channels with 50-μm intervals and scanned 20 times at the speed of 100 mm/s was completed within 16 s. The width of the channels ($a = 25.3 \pm 0.4$ μm) was perfectly uniform, indicating the accurate CGH calculation using the GS algorithm. Diffractive efficiency has been measured as ~50%, allowing >1.2 W diffracted into 25 parallel beams. This has the effect of creating an "effective" repetition rate of 500 kHz without restrictive scan speed of a galvanometer.

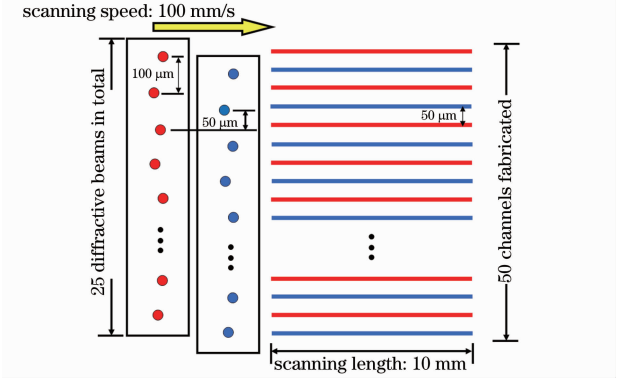

Fig. 39 Schematic showing the design of the 25 beams pattern and the method of scanning (the vertical distance between two adjacent spots was 100 μm; by repeatedly scanning the pattern with 50-μm vertical offset each time, multiple micro-channels with 50-μm intervals can be obtained)[42]

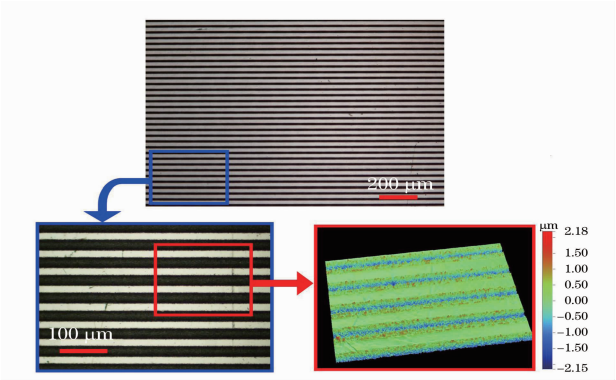

Fig. 40 Micro-graph demonstrating the results of micro-channels covering a (10 mm × 10 mm) area machined by the 25 beams pattern on polished Ti6Al4V (upper), and micro-graphs showing the result with higher magnification (lower left) and 3D surface profile image by Wyko NT1100 optical surface profiler (lower right)[42]

As demonstrated above, the distortion of intensity profile at high diffraction angle is eliminated due to the narrower spectral bandwidth of the laser source. The drilled holes can perfectly keep their round shape (eccentricity: $e < 1.04$) when applying large diffraction angle ($\theta \approx 1.27°$). High power (2.5 W) parallel processing with 25 diffracted beams and laser repetition rate applied ($f \approx 20$ kHz), demonstrates industrial level precision laser micro-processing.

6 Diffractive Multi-beam Internal Structuring with Femto-second Laser

Multi-photon induced refractive index (RI) change Δn of optical materials has been suggested as a route to the creation of complex 3D integrated optical circuits[71]. Temporal pulse duration of <100 fs in the NIR shows clear advantages for generating highest Δn in, for example, fused silica and polymethyl methacrylate (PMMA)[5]. While for temporal pulse duration of >160 fs, where optical breakdown is increasingly more likely, second harmonic ultraviolet (UV) refractive index modification of PMMA overcomes this limitation by reducing the order of non-linear absorption from three to two-photon[7]. Laser repetition rates from kHz to MHz have been used for Δn structuring and this parameter is also important in determining the sign of refractive index change[72], while integrated fluence

exposure still needs to be comparable. For example, at 1 kHz, NIR single pulse energy $E_p < 1$ μJ/pulse is typically tightly focussed inside an optical substrate while $E_p > 1$ mJ/pulse is generally available, a light utilisation factor of $< 0.1\%$. At 1 kHz, Δn in PMMA (and fused silica) has been clearly shown to be positive, essential for single mode waveguides[7]. Phase gratings, optical waveguides, and couplers have previously been demonstrated with single point femto-second processing in a wide range of materials[71, 73, 74], however the extension to complex 3D optical circuits may be significantly hampered, particularly as modification depths reach ~10 μm when a high numerical aperture (NA) objective is used.

A SLM is a remarkable dynamic diffractive optical element able to create a desired optical landscape through sophisticated control of the phase of an incident high intensity laser beam. Here, highly parallel refractive index structuring inside optical materials by combining a kHz femto-second laser system with a SLM and thus generating a myriad of low fluence diffracted beams through applying CGHs was demonstrated. Calculations based on the GS algorithms are used to generate the required phase patterns within a LabVIEW environment[53]. Consequently, the time for the fabrication of RI optical engineering could be reduced from hours to minutes with a gain factor of $G > 10$, opening up new possibilities in optical circuit manufacture.

6.1 Experimental Setup

Figure 41 shows a schematic of the experimental setup for internal structuring. The output from a Clark-MXR 2010 femto-second laser system (775 nm, 160 fs, 1 kHz) was passed through a pick off (Autocorrelator) and 50/50 ultra-fast beam splitter to turning mirror M1 then attenuated and expanded

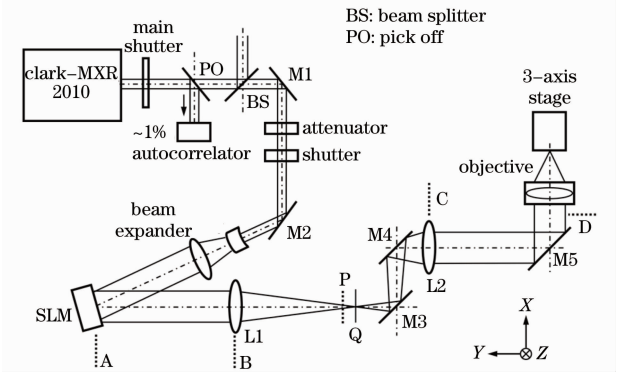

Fig. 41 Schematic of experimental system[42]

onto a Hamamatsu X10468-01 SLM. A 4f optical system consisting of two plano-convex lenses L1 and L2 ($f_1 = f_2 = 300$ mm) re-imaged the surface of the SLM to the input aperture of a microscope objective (Nikon, 0.15 NA) allowing the blocking of the remaining energetic zero order reflection near the Fourier plane (Q) of lens L1 by using a small target.

Diffracted beams correspond to higher spatial frequencies and consequently focus off axis as much as ~5 mm from the optic axis at plane P. From the desired intensity distribution at the focal plane of the objective, the corresponding CGH was calculated and applied to the SLM and the resulting phase pattern (8-bit greyscales) observed on a separate monitor elucidating the phase distribution on the SLM. The transparent substrates were scanned transversely, as shown in Fig. 42, to create 2D and 3D structures. Therefore, there can be more than 10 near identical beams in parallel at any one time.

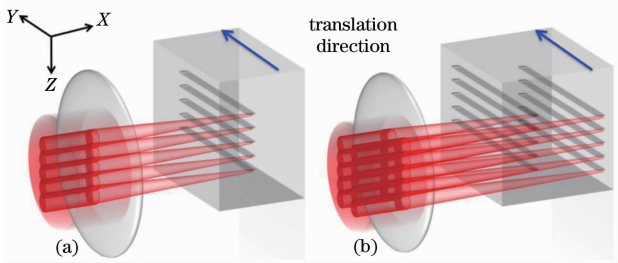

Fig. 42 Schematics showing transverse geometry for writing of gratings in (a) 2D single layer and (b) 3D double layer. The blue arrows denote the stage translation direction[75]

Previous study has demonstrated that the symmetry of multiple beams can greatly affect the intensity distribution across all beams[68]. Figure 43(a) shows a common multi-beam pattern with perfect symmetry for parallel processing. However, the symmetric multi-beam suffers from low intensity uniformity even using iterative algorithm like GS (~60%)[76]. One approach to solve this problem is to introduce a small amount of random displacement to the multi-beam pattern, since for most algorithms such as GS, GL, and the generalized adaptive additive algorithm (GAA), spatial randomization can significantly reduce intensity variation[68]. For example, the random displacement can be applied to the Y direction, while the separation Λ in the Z direction is fixed, as shown in Fig. 43(b), in order to optimize energy distribution across the multi-beam. Another method is to use the weighted Gerchberg-Saxton

(GSW) algorithm[76], which can provide >90% uniformity even with a symmetric pattern. However, the calculation speed of GSW is slower than that of GS.

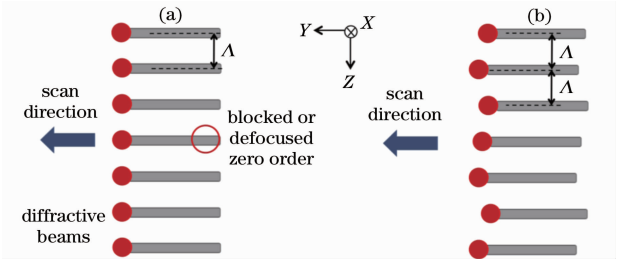

Fig. 43 Schematics of (a) a symmetric and (b) an asymmetric multi-beam pattern for parallel processing[75]

6.2 Static Multi-beam Parallel Direct Writing

Parallel RI modification with 12 nearly uniform beams with a pitch Λ of 35 μm is shown in the optical micro-graphs of Fig. 44. Pulse energy E_p was 0.6 μJ/beam. Transverse scan speed was 1 mm/s and each modified region was scanned once only. Clear RI modification without optical breakdown was obtained.

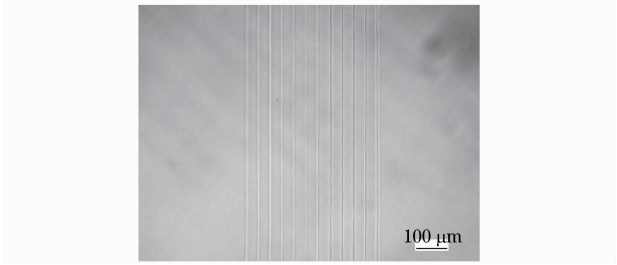

Fig. 44 12 beams direct writing in a PMMA sample

By recalculating the CGHs to offset the focal planes of particular spots, simultaneous parallel 3D writing at different depths using 10 (5×2) beams in a double layer was demonstrated, as shown in Fig. 45. The writing parameters are the same as that used in Fig. 44.

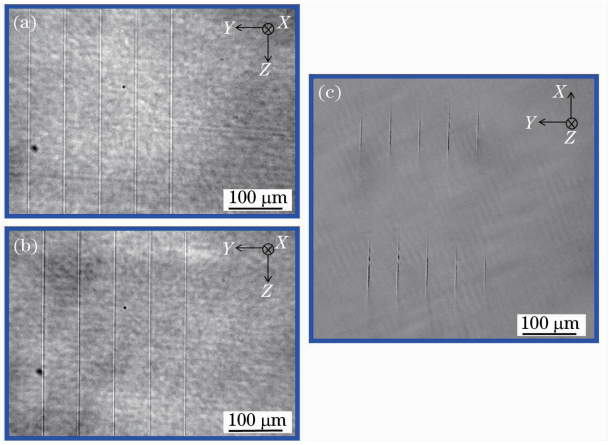

Fig. 45 10 (5×2) beams 3D direct writing in a PMMA sample, (a) front view of the top layer, (b) front view of the bottom layer, and (c) cross section of two layers. The laser beams propagate along the +X direction[75]

6.3 Dynamic Multi-beam 3D Direct Writing

Dynamic modification of fused silica with 5 beams (0, ±1st, and ±2nd order), which are generated by a binary grating, is demonstrated in Fig. 46. The helical structures were produced by synchronising rotation of 5 beams through real-time display of 120 pre-calculated CGHs at 20 Hz and 3° interval with linear motion of the stage towards the +X direction at 0.5 mm/s. The laser beams with pulse energies of 1.5 μJ/beam propagated along the +X axis.

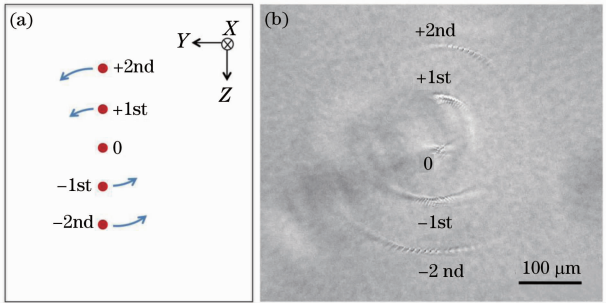

Fig. 46 Five beams including 0, ±1st, and ±2nd order dynamic structuring of fused silica. (a) Schematic diagram with the arrows indicating the rotation direction of the beams; (b) micro-graph of the modified region

7 Applications

Since sufficient laser output from commercial laser sources is currently exceeding single beam process requirements, parallel processing with multiple beams could provide an easy route for up-scaling processing speed and suppress manufacturing costs. The methods described for parallel processing of materials with high speed, dynamic control, and great flexibility, facilitate applications in the following areas.

7.1 Silicon Wafer Scribing

Figure 47 depicts the microscopic image of a silicon sample that was scribed using 15 asymmetric beams produced by using the X10468-04 SLM at 532-nm wavelength, 10-ps pulselength, and 5-kHz repetition rate. The 15 beams with total incident pulse energy of 21 μJ (1.4 μJ/beam), were scanned orthogonally with two CGHs at 10 mm/s to produce the cross hatched pattern. The scribe lines were ~500-nm deep and 14-μm wide with the pitch

Λ of 86 μm. No thermal damage to the surrounding area can be observed.

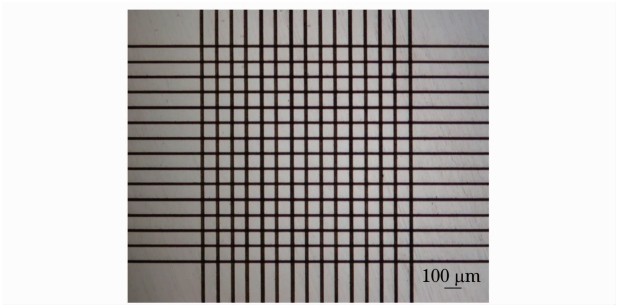

Fig. 47 Multi-beam parallel processing of a silicon sample[43]

Beam scanning with a different number of spots per line mimics a variable spot overlap and can produce variable controlled ablation depth, as presented in Fig. 48. Ten beams were arranged in a 4-3-2-1 pattern so as to achieve selective ablation with a single scan at different positions. The small circles in Fig. 48(b) denotes the 10-beam pattern used for silicon scribing. The total pulse energy (E_p) incident on the sample was 18 μJ, hence giving $E_p \sim 1.8$ μJ to each of the diffractive beams. Figures 48(b) and (c) demonstrate the machining results on a silicon wafer with 532-nm laser wavelength, 5-kHz repetition rate, and 1-mm/s scanning speed, where different ablation depths

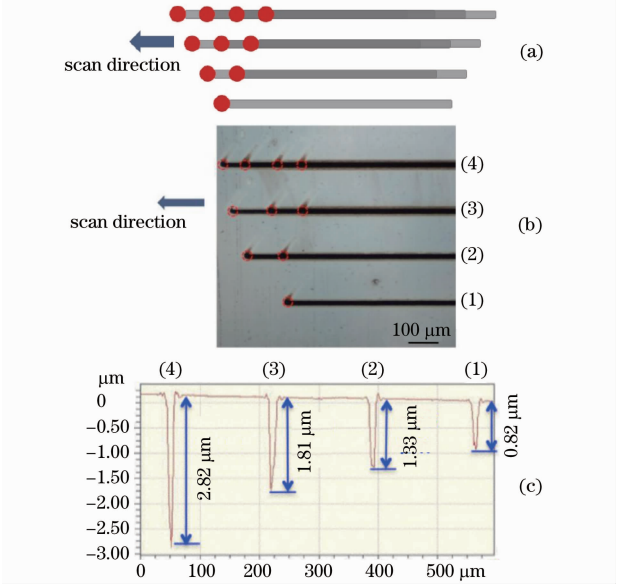

Fig. 48 (a) Schematic of selective ablation using a different number of spots per line to produce different ablation depth; (b) micro-graph of 10 beams selective ablation on silicon. The circles represent the positions of the 10 beams; (c) cross-sectional of surface profile of the 10 beam selective ablation on silicon. The scribe line 1, 2, 3, and 4 are consistent with those labelled in (b)[43]

were obtained.

7.2 Patterning of Organic Light Emitting Diodes Materials

Laser patterning of organic light emitting diode (OLED) is a key industrial process in the manufacturing of OLED displays or solid-state lighting foils[77]. Ultra-fast lasers are of particular interest for this application as they enable selective ablative removal of OLED layers with very low energy density requirements on the target. Since laser output from commercial laser sources is currently exceeding single beam process requirements, parallel processing with multiple beams could provide a novel route for up-scaling processing speed and reduce manufacturing costs. Hence SLMs could be employed for high throughput precision patterning of OLED materials (metal cathode and ITO anode) on flexible and glass substrates.

7.2.1 Cathode Patterning

Since OLEDs are multi-layer materials, and each layer has different ablation threshold, (e.g., the top cathode layer, aluminium, has lower ablation threshold than the underlying anode layer, ITO film[78]), it is important to control the laser fluence so that it is high enough to completely remove aluminium, but is lower than the ablation threshold of the ITO. Multi-beam scribing of an OLED sample using 15 beams with 532-nm wavelength produced by the X10468-04 SLM is shown in Fig. 49. The laser pulse energy, repetition rate, and scanning speed were 12 μJ, 5 kHz, and 30 mm/s, respectively. Only a single scan was conducted, resulting in multiple scribing lines with the pitch of 86 μm, a line width of $\sim$10 μm and the depth of $\sim$300 nm, which is the interface between the organic layer and the anode.

7.2.2 Anode (ITO) Patterning

Since the absorption of ITO material in the NIR region is stronger than that in the visible region, a pico-second laser with a wavelength of 1064 nm was used for patterning of ITO on glass samples. Figure 50 demonstrates a microscope image and surface profile of the ITO sample that was ablated using 5 beams generated by a Hamamatsu X10468-03 SLM with 1064-nm wavelength. The incident pulse energy on the sample was 16 μJ with 5-kHz repetition rate, 15-mm/s scanning speed. Only a single scan was performed. The pitch Λ was 65 μm. As illustrated, the scribing line had a depth of $\sim$60 nm and a width of 14 μm, and showed a flat bottom area in-

dicating complete removal of the ITO film. Placing the spots closer and using lower laser pulse energies can reduce the pitch and the scribing width, respectively. There was no thermal damage to the surrounding area observed.

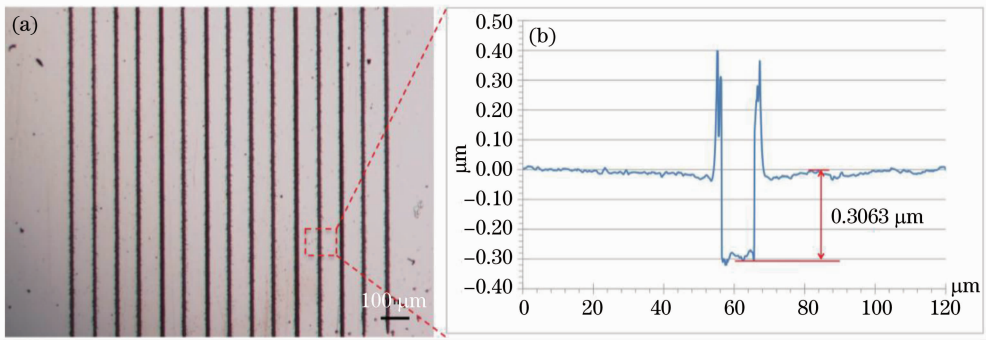

Fig. 49 Parallel processing of an OLED sample using 15 beams. (a) optical micrographs; (b) cross-sectional profile of a single scribing line[43]

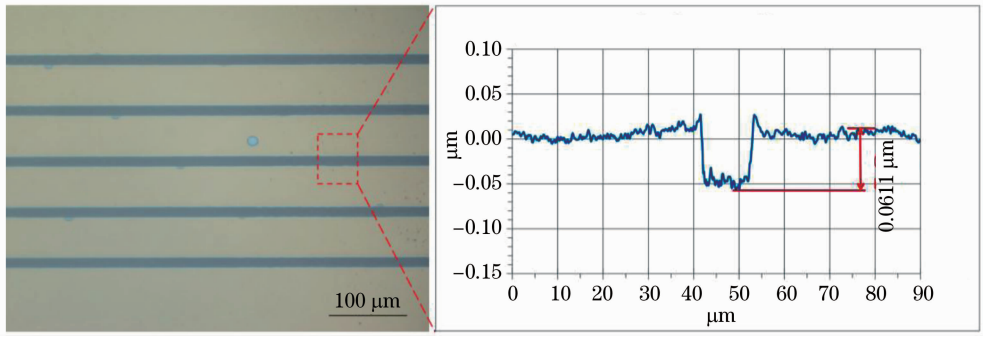

Fig. 50 Parallel processing of ITO thin film sample using 5 beams. (a) optical micrographs; (b) cross-sectional profile of a single scribe

7.3 Direct Writing of Volume Grating

Using 21 beams, a series of 5 mm×5 mm×1 mm gratings with 19-μm period were written in PMMA, as shown in Fig. 51, with each one fabricated in less than 10 minutes[79]. A diffractive pattern with 21 desired diffractive beams, as shown in the Fig. 52, was used for the parallel processing, hence greatly increasing the fabrication speed. Each of the gratings was completed within 10 minutes. The diffraction efficiency ~68% at the Bragg angle indicates that $\Delta n \sim 1.64 \times 10^{-4}$, according to Kogelnik's coupled wave theory[80]. The gain in writing speed has the effect of multiplying the laser repetition rate by the gain factor G without the drawbacks of higher frequencies such as increased thermal accumulation

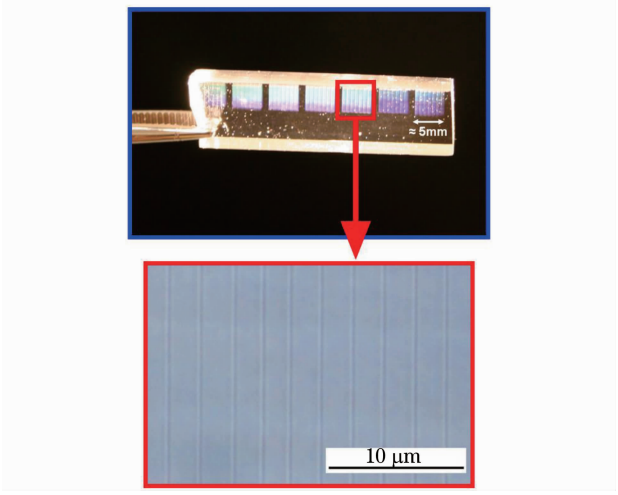

Fig. 51 A series of volume gratings written inside a PMMA slab and a magnified optical micrograph

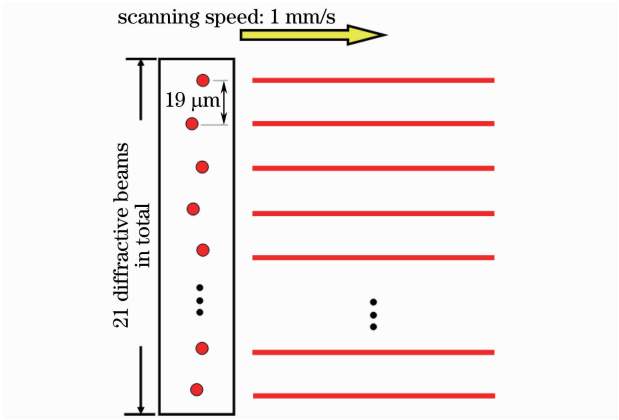

Fig. 52 Schematic showing the diffractive pattern with 21 desired diffractive beams. The volume grating was fabricated at a scanning speed of 1 mm/s

effects and the necessity of increased scan speeds of the substrate, ultimately hitting inertial limits of motion control stages. By integrating objectives with $0.15<NA<0.5$, the route is open to fabricate a wide range of internal optical components including waveguides, couplers, gratings, and Fresnel lenses at unprecedented speed.

8 Conclusions and Future Work

In condusion, this paper demonstrates multi-beam ultra-fast laser parallel micro-processing using a SLM. The desired diffractive beam patterns are modulated by CGHs, calculated by appropriate algorithms. The zero order beam, which otherwise might cause undesired damage, can be either blocked at the Fourier plane by installing a $4f$ optical system or defocused at the processing plane by adding a Fresnel zone lens onto the CGH. The surface structuring of semiconductors and metals using multi-beam patterns synchronised with a scanning galvanometer system shows flexible and high throughput parallel processing. By highly focusing the diffractive beams using an objective into optical materials, dynamic 2D and 3D internal structuring has been demonstrated. The results reveals high precision micro-processing with higher efficiency, showing the potential of ultra-fast laser parallel processing in industrial applications.

Future work will be focussed on testing the power handling capability of the SLMs, hence exploring the maximum viable energy diffracted to the desired multi-beam, which is a significant step of transferring this parallel processing technique from laboratory to industry.

Acknowledgments

The authors gratefully acknowledge the support of the North West Development Agency (NWDA) and the Technology Strategy Board (TSB) under the project PARALASE (No. TP11/LLd/6/I/AF063B), and the kind help from Prof. Miles Padgett and Dr. Jonathan Leach in the Department of Physics and Astronomy at the University of Glasgow, Scotland. The authors also thank Prof. Minlin Zhong for the invitation to write this paper for the Chinese Journal of Lasers. One of the authors, Zheng Kuang, would like to thank the Scholarship of Overseas Research Students Award Scheme (ORSAS) and the University of Liverpool Graduate Association (Hong Kong) for providing financial support for his PhD study at the University of Liverpool.

References

1 D. Du, X. Liu, G. Korn *et al*.. Laser-induced breakdown by impact ionization in SiO_2 with pulse widths from 7 ns to 150 fs[J]. *Appl. Phys. Lett.*, 1994, **64**: 3071～3073

2 X. Liu, D. Du, G. Mourou. Laser ablation and micromachining with ultrashort laser pulses[J]. *IEEE J. Quantum Electron.*, 1997, **33**: 1706～1716

3 B. N. Chichkov, C. Momma, S. Nolte *et al*.. femto-second, pico-second and nanosecond laser ablation of solids[J]. *Appl. Phys. A*, 1996, **63**: 109～115

4 F. Dausinger. Machining of metals with ultrashort laser pulses: from fundamental investigations to industrial applications[C]. *SPIE*, 2005, **5777**: 840

5 A. Baum, P. J. Scully, W. Perrie *et al*.. Pulse-duration dependency of femtosecond laser refractive index modification in poly (methyl methacrylate)[J]. *Opt. Lett.*, 2008, **33**: 651～653

6 H. Guo, H. Jiang, Y. Fang *et al*.. The pulse duration dependence of femtosecond laser induced refractive index modulation in fused silica[J]. *J. Opt. A: Pure Appl. Opt.*, 2004, **6**: 787～790

7 A. Baum, P. J. Scully, M. Basanta *et al*.. Photochemistry of refractive index structures in poly(methyl methacrylate) by femtosecond laser irradiation[J]. *Opt. Lett.*, 2007, **32**: 190～192

8 R. Le. Harzic, D. Breitlung, M. Weikert *et al*.. Pulse width and energy influence on laser micromachining of metals in a range of 100 fs to 5 ps[J]. *Appl. Surf. Sci.*, 2005, **249**: 322～331

9 W. Perrie, M. Gill, G. Robinson *et al*.. Femtosecond laser microstructuring of aluminium under helium[J]. *Appl. Surf. Sci.*, 2004, **230**: 50～59

10 A. Luft, U. Franz, A. Emsemann *et al*.. A study of thermal and mechanical effects on materials induced by pulsed laser drilling [J]. *Appl. Phys. A*, 1996, **63**: 93～101

11 K. Kawamura, T. Ogawa, N. Sarukura *et al*.. Fabrication of surface relief gratings on transparent dielectric materials by two-beam holographic method using infrared femtosecond laser pulses[J]. *Appl. Phys. B*, 2000, **71**: 119～121

12 T. Kondo, S. Matsuo, S. Juodkazis *et al*.. A novel femtosecond laser interference technique with diffractive beam splitter for fabrication of three-dimensional photonic crystals[J]. *Appl. Phys. Lett.*, 2001, **79**: 725～727

13 T. Kondo, S. Matsuo, S. Juodkazis *et al*.. Multiphoton fabrication of periodic structures by multibeam interference of femtosecond pulses[J]. *Appl. Phys. Lett.*, 2003, **82**: 2758～2760

14 S. Yang, M. Megens, J. Aizenberg *et al*.. Creating periodic three-dimensional structures by multibeam interference of visible laser[J]. *Chem. Mater.*, 2002, **14**: 2831～2833

15 H. Misawa, T. Kondo, S. Juodkazis *et al*.. Holographic lithography of periodic two- and three-dimensional microstructures in photoresist SU-8[J]. *Opt. Express*, 2006, **14**: 7943～7953

16 S. Shoji, R. Zaccaria, H. B. Sun *et al*.. Multi-step multi-beam laser interference patterning of three-dimensional photonic lattices [J]. *Opt. Express*, 2006, **14**: 2309～2316

17 S. Shoji, S. Kawata. Photofabrication of three-dimensional photonic crystals by multibeam laser interference into a photopolymerizable resin[J]. *Appl. Phys. Lett.*, 2000, **76**: 2668～2670

18 S. Shoji, H. B. Sun, S. Kawata. Photofabrication of wood-pile three-dimensional photonic crystals using four-beam laser interference[J]. *Appl. Phys. Lett.*, 2003, **83**: 608～610

19 M. Campbell, D. N. Sharp, M. T. Harrison *et al*.. Fabrication of photonic crystals for the visible spectrum by holographic lithogra-

phy[J]. *Nature*, 2000, **404**: 53～56
20 Y. Li, W. Watanabe, K. Yamada *et al*.. Holographic fabrication of multiple layers of grating inside soda-lime glass with femtosecond laser pulses[J]. *Appl. Phys. Lett.*, 2002, **80**: 1508～1510
21 K. Venkatakrishnan, N. R. Sivakumar, C. W. Hee *et al*.. Direct fabrication of surface-relief grating by interferometric technique using femtosecond laser[J]. *Appl. Phys. A*, 2003, **77**: 959～963
22 Y. Nakata, T. Okada, M. Maeda. Nano-sized hollow bump array generated by single femtosecond laser pulse[J]. *Jpn. J. Appl. Phys.*, 2003, **42**: L1452～L1454
23 Y. Nakata, T. Okada, M. Maeda. Fabrication of dot matrix, comb, and nanowire structures using laser ablation by interfered femtosecond laser beams[J]. *Appl. Phys. Lett.*, 2002, **81**: 4239～4241
24 Y. Nakata, T. Okada, M. Maeda. Formation of periodic structure inside silica glass and acryl by interfering femtosecond laser[J]. *Jpn. J. Appl. Phys.*, 2003, **42**: L379～L380
25 Y. Nakata, T. Okada, M. Maeda. Lines of periodic hole structures produced by laser ablation using interfering femtosecond lasers split by a transmission grating[J]. *Appl. Phys. A*, 2003, **77**: 399～401
26 S. Matsuo, T. Miyamoto, T. Tomita *et al*.. Applications of a microlens array and a photomask to the laser microfabrication of a periodic photopolymer rod array[J]. *Appl. Opt.*, 2007, **46**: 8264～8267
27 M. Oikawa, K. Iga. Distributed-index planar microiens[J]. *Appl. Opt.*, 1982, **21**: 1052～1056
28 S. Matsuo, S. Juodkazis, H. Misawa. Femtosecond laser microfabrication of periodic structures using a microlens array[J]. *Appl. Phys. A*, 2005, **80**: 683～685
29 J. Kato, N. Takeyasu, Y. Adachi *et al*.. Multiple-spot parallel processing for laser micronanofabrication[J]. *Appl. Phys. Lett.*, 2005, **86**: 044102～044104
30 C. H. Sow, A. A. Bettiol, Y. Y. G. Lee *et al*.. Multiple-spot optical tweezers created with microlens arrays fabricated by proton beam writing[J]. *Appl. Phys. B*, 2004, **78**: 705～710
31 Z. B. Wang, W. Guo, A. Pena *et al*.. Laser micro/nano fabrication in glass with tunable-focus particle lens array[J]. *Opt. Express*, 2008, **16**: 19706～19711
32 Y. Hayasaki, T. Sugimoto, A. Takita *et al*.. Variable holographic femtosecond laser processing by use of a spatial light modulator [J]. *Appl. Phys. Lett.*, 2005, **87**: 031101～031103
33 S. Hasegawa, Y. Hayasaki, N. Nishida. Holographic femtosecond laser processing with multiplexed phase Fresnel lenses[J]. *Opt. Lett.*, 2006, **31**: 1705～1707
34 Y. Kuroiwa, N. Takeshima, Y. Narita *et al*.. Arbitrary micropatterning method in femtosecond laser microprocessing using diffractive optical elements[J]. *Opt. Express*, 2004, **12**: 1908～1915
35 H. Takahashi, S. Hasegawa, Y. Hayasaki. Holographic femtosecond laser processing using optimal-rotation-angle method with compensation of spatial frequency response of liquid crystal spatial light modulator[J]. *Appl. Opt.*, 2007, **46**: 5917～5923
36 H. Takahashi, S. Hasegawa, A. Takita *et al*.. Sparse-exposure technique in holographic two-photon polymerization[J]. *Opt. Express*, 2008, **16**: 16592～16599
37 Y. Hayasaki. Holographic femtosecond laser processing and three-dimensional recording in biological tissues[C]. Progress In Electromagnetics Research Letters, 2008, **2**: 115～123
38 S. Hasegawa, Y. Hayasaki. Holographic femtosecond laser processing with multiplexed phase fresnel lenses displayed on the liquid crystal spatial light modulator[J]. *Opt. Rev.*, 2007, **14**: 208～213
39 K. Chaen, H. Takahashi, S. Hasegawa *et al*.. Display method with compensation of the spatial frequency response of a liquid crystal spatial light modulator for holographic femtosecond laser processing[J]. *Opt. Commun.*, 2007, **280**: 165～172
40 Z. Kuang, W. Perrie, J. Leach *et al*.. High throughput diffractive multi-beam femtosecond laser processing using a spatial light modulator[J]. *Appl. Surf. Sci.*, 2008, **255**: 2284～2289
41 Z. Kuang, D. Liu, W. Perrie *et al*.. Fast parallel diffractive multi-beam femtosecond laser surface micro-structuring [J]. *Appl. Surf. Sci.*, 2009, **255**: 6582～6588
42 Z. Kuang, W. Perrie, D. Liu *et al*.. Diffractive multi-beam surface micro-processing using 10 ps laser pulses[J]. *Appl. Surf. Sci.*, 2009, **255**: 9040～9044
43 D. Liu, Z. Kuang, S. Shang *et al*.. ultra-fast parallel laser processing of materials for high throughput manufacturing[C]. Proceedings of LAMP2009——the 5th International Congress on Laser Advanced Materials Processing, 2009, Kobe, Japan
44 http://www.holoeye.com/spatial_light_modulator_lc_r_2500.html accessed in September 2009
45 http://jp.hamamatsu.com/products/division/crl/1010/X10468/index_en.html accessed in Septermber 2009
46 U. Efron. Spatial light modulator technology: materials, devices, and applications, Marcel Dekker, Inc. 1995
47 I. C. Khoo. Liquid crystals[M]. John Wiley & Sons. Inc. 2nd edition, 2007
48 Phase and amplitude modulation properties of the LC-R 2500, Manual of Holoeye SLM (LC-R2500)
49 J. Leach, G. Sinclair, P. Jordan *et al*.. 3D manipulation of particles into crystal structures using holographic optical tweezers[J]. *Opt. Express*, 2004, **12**: 220～226
50 G. Sinclair, J. Leach, P. Jordan *et al*.. Interactive application in holographic optical tweezers of a multi-plane Gerchberg-Saxton algorithm for three-dimensional light shaping[J]. *Opt. Express*, 2004, **12**: 1665～1670
51 G. Whyte, G. Gibson, J. Leach *et al*.. An optical trapped microhand for manipulating micron-sized objects[J]. *Opt. Express*, 2006, **14**: 2497～12502
52 M. Reicherter, S. Zwick, T. Haist *et al*.. Fast digital hologram generation and adaptive force measurement in liquid-crystal-display-based holographic tweezers[J]. *Appl. Opt.*, 2006, **45**: 888～896
53 J. Leach, K. Wulff, G. Sinclair *et al*.. Interactive approach to optical tweezers control[J]. *Appl. Opt.*, 2006, **45**: 897～903
54 J. Liesener, M. Reicherter, T. Haist *et al*.. Multi-functional optical tweezers using computer-generated holograms[J]. *Opt. Commun.*, 2000, **185**: 77～82
55 G. Gibson, D. M. Carberry, G. Whyte *et al*.. Holographic assembly workstation for optical manipulation[J]. *J. Opt. A: Pure Appl. Opt.*, 2008, **10**: 044009
56 J. A. Grieve, A. Ulcinas, S. Subramanian *et al*.. Hands-on with optical tweezers: a multitouch interface for holographic optical trapping[J]. *Opt. Express*, 2009, **17**: 3595～3602
57 P. Jordan, J. Leach, M. Padgett *et al*.. Creating permanent 3D arrangements of isolated cells using holographic optical tweezers [J]. *Lab on a Chip*, 2005, **5**: 1224～1228
58 M. Reicherter, T. Haist, E. U. Wagemann *et al*.. Optical particle trapping with computer-generated holograms written on a liquid-crystal display[J]. *Opt. Lett.*, 1999, **24**: 608～610
59 A. Horst, N. R. Forde. Calibration of dynamic holographic optical tweezers for force measurements on biomaterials[J]. *Opt. Express*, 2008, **16**: 20987～21003
60 P. C. Mogensen, J. Glückstad. Dynamic array generation and pattern formation for optical tweezers[J]. *Opt. Commun.*, 2000, **175**: 75～81
61 G. Sinclair, P. Jordan, J. Leach *et al*.. Defining the trapping limits of holographical optical tweezers[J]. *J. Mod. Opt.*, 2002, **51**: 409～414
62 H. Melville, G. Milne, G. Spalding *et al*.. Optical trapping of

three-dimensional structures using dynamic holograms[J]. *Opt. Express*, 2003, **11**: 3562～3567

63 J. E. Curtis, B. A. Koss, D. G. Grier. Dynamic holographic optical tweezers[J]. *Opt. Commun.*, 2002, **207**: 169～175

64 D. G. Grier. A revolution in optical manipulation[J]. *Nature*, 2003, **424**: 810～816

65 O. Samek, V. Hommes, R. Hergenröder *et al*.. Femtosecond pulse shaping using a liquid-crystal display: applications to depth profiling analysis[J]. *Rev. Sci. Instrum.*, 2005, **76**: 086104

66 A. M. Weiner. Femtosecond pulse shaping using spatial light modulators[J]. *Rev. Sci. Instrum.*, 2000, **71**: 1929～1960

67 R. W. Gerchberg, W. O. Saxton. A practical algorithm for the determination of the phase from image and diffraction plane pictures[J]. *Optik*, 1972, **35**: 237～246

68 J. E. Curtis, C. H. J. Schmitz, J. P. Spatz. Symmetry dependence of holograms for optical trapping[J]. *Opt. Lett.*, 2005, **30**: 2086～2088

69 T. Haist, E. U. Wagemann, H. J. Tiziani. Pulsed-laser ablation using dynamic computer-generated holograms written into a liquid crystal display[J]. *J. Opt. A: Pure Appl. Opt.*, 1999, **1**(3): 428～430

70 T. Haist, M. Schönleber, H. J. Tiziani. Computer-generated holograms from 3D-objects written on twisted－nematic liquid crystals displays[J]. *Opt. Commun.*, 1997, **140**: 299～308

71 P. J. Scully, D. Jones, D. A. Jaroszynski. Femtosecond laser irradiation of polymethyl methacrylate for refractive index gratings [J]. *J. Opt. A*, 2003, **5**: S92～S96

72 A. Zoubir, C. Lopez, M. Richardson *et al*.. Femtosecond laser fabrication of tubular waveguides in poly(methyl methacrylate) [J]. *Opt. Lett.*, 2004, **29**: 1840～1842

73 K. M. Davis, K. Miura, N. Sugimoto *et al*.. Writing waveguides in glass with a femtosecond laser[J]. *Opt. Lett.*, 1996, **21**: 1729～1731

74 D. Homoelle, S. Wielandy, A. L. Gaeta *et al*.. Infrared photosensitivity in silica glasses exposed to femtosecond laser pulses [J]. *Opt. Lett.*, 1999, **24**: 1311～1313

75 D. Liu, Z. Kuang, W. Perrie *et al*.. High speed ultrafast 3D refractive index micro-structuring of poly(methyl methacrylate)[J], manuscript under preparation

76 R. D. Leonardo, F. Ianni, G. Ruocco. Computer generation of optimal holograms for optical trap arrays[J]. *Opt. Express*, 2007, **15**: 1913～1922

77 S. R. Forrest. The path to ubiquitous and low-cost organic electronic appliances on plastic[J]. *Nature*, 2004, **428**: 911～918

78 C. Liu, G. Zhu, D. Liu. Patterning cathode for organic light-emitting diode by pulsed laser ablation[J]. *Displays*, 2008, **29**: 536～540

79 P. J. Scully, A. Baum, D. Liu *et al*.. Part Ⅲ Chapter 12——Refractive index structures in polymers, Springer book——Femtosecond laser micromachining: photonic and microfluidic devices in transparent materials. To be published in 2010

80 H. Kogelnik. Coupled Wave Theory for Thick Hologram Gratings [J]. *Bell Syst. Tech. J.*, 1969, **48**: 2909